

# GRAVOTURBULENT PLANETESIMAL FORMATION: THE POSITIVE EFFECT OF LONG-LIVED ZONAL FLOWS

K. DITTRICH<sup>1</sup>, H. KLAHR<sup>1</sup>, AND A. JOHANSEN<sup>2</sup>

<sup>1</sup>Max-Planck-Institut für Astronomie, Königstuhl 17, D-69117 Heidelberg, Germany and

<sup>2</sup>Lund Observatory, Department of Astronomy and Theoretical Physics, Box 43, SE-22100 Lund, Sweden

*Draft version January 10, 2013*

## ABSTRACT

Recent numerical simulations have shown long-lived axisymmetric sub- and super-Keplerian flows in protoplanetary disks. These zonal flows are found in local as well as global simulations of disks unstable to the magnetorotational instability. This paper covers our study of the strength and lifetime of zonal flows and the resulting long-lived gas over- and underdensities as functions of the azimuthal and radial size of the local shearing box. We further investigate dust particle concentrations without feedback on the gas and without self-gravity. Strength and lifetime of zonal flows increases with the radial extent of the simulation box, but decreases with the azimuthal box size. Our simulations support earlier results that zonal flows have a natural radial length scale of 5 to 7 gas pressure scale heights. This is the first study that combines three-dimensional MHD simulations of zonal flows and dust particles feeling the gas pressure. The pressure bumps trap particles with  $St = 1$  very efficiently. We show that  $St = 0.1$  particles (of some centimeters in size if at 5 AU in an MMSN) reach a hundred-fold higher density than initially. This opens the path for particles of  $St = 0.1$  and dust-to-gas ratio of 0.01 or for particles of  $St \geq 0.5$  and dust-to-gas ratio  $10^{-4}$  to still reach densities that potentially trigger the streaming instability and thus gravoturbulent formation of planetesimals.

*Subject headings:* magnetohydrodynamics (MHD) - planets and satellites: formation - protoplanetary disks

## 1. INTRODUCTION

Planets form as a side product in star formation. The general understanding on how planets in our solar system form was detailed in Safronov (1969). Low-mass stars form out of molecular clouds which consist of 99% hydrogen and helium (further referred to as gas), and 1% dust and ices (Lodders 2003), i.e., everything that has a higher complexity than hydrogen molecules or helium. Those molecular clouds have cores between less than  $0.1M_{\odot}$  and more than  $10M_{\odot}$  (Krumholz et al. 2012) that are gravitationally unstable. Most parts of the mass will collapse into a newborn star. The remaining  $\sim 1\%$  of the total mass will form an accretion disk with pressure supported, sub-Keplerian gas (Weidenschilling 1977a; Cassen & Moosman 1981) around the young star. Those disks have lifetimes in the order of a few million years (Haisch et al. 2001; Fedele et al. 2010). Dust particles grow due to coagulation (Weidenschilling 1997). However, coagulation models show that there are several barriers to overcome to grow dust large enough to become gravitationally bound in kilometer-sized planetesimals, such as the bouncing barrier (Zsom et al. 2010; Windmark et al. 2012a,b), the fragmentation barrier (e.g., Beitz et al. 2011; Birnstiel et al. 2012, and references therein), and the kilometer-size barrier (Ida et al. 2008; Cuzzi et al. 2008). Dust growth mechanisms are summarized in Dominik et al. (2007) and the review of Blum & Wurm (2008) gives an overview on the mentioned barriers.

This paper addresses the fragmentation barrier or meter-size barrier. Pebbles of several decimeters in size will drift very fast inward due to the headwind from the

sub-Keplerian gas (Weidenschilling 1977a). Thus, dust has to grow very quickly from some centimeters to several kilometers in size in order to avoid drifting into the inner region of the protoplanetary disk.

Turbulence in protoplanetary disks around young stars provides promising mechanisms for rapid planetesimal formation (Johansen et al. 2007, 2011). Shearing box simulations (Brandenburg et al. 1995) are a powerful tool for analyzing the magnetorotational instability (MRI; Balbus & Hawley 1991, 1998) as a source of turbulence. These simulations consider a local, corotating box, representing a small part of a Keplerian disk. Johansen et al. (2009a) reported long-lived axisymmetric sub- and super-Keplerian flows, zonal flows, in shearing box simulations of turbulence caused by the MRI. These zonal flows have been seen in several other local (Fromang & Stone 2009; Stone & Gardiner 2010; Simon et al. 2012) and global (Lyra et al. 2008; Dzyurkevich et al. 2010; Uribe et al. 2011; Flock et al. 2011, 2012) simulations using a wide variety of codes.

Zonal flows are a product of large-scale variations in the magnetic field that transport momentum differentially, creating regions of slightly faster and slightly slower rotating gas. Large-scale pressure bumps are excited through geostrophic balance. This creates long-lived over-densities that potentially trap dust particles. A more thorough description of zonal flows and their creation put forward in Johansen et al. (2009a) found zonal flows always populating the largest radial mode available in the local box approximation. Their largest box was simulating 10.56 pressure scale heights ( $H$ ). More recently Simon et al. (2012) found a more complex structure in their largest simulation with  $L_x = 16H$ . They further studied the autocorrelation function (Guan et al.

2009) of the magnetic field and the gas density. Both have a two-component structure. The first is tilted with respect to the azimuthal axis and highly localized. The second component is seen at the largest scales and can be associated with the (predominantly toroidal) background magnetic field. Simon et al. (2012) measure the radial length scale of the zonal flows to converge at  $6H$ .

In this paper we consider even larger physical extents for zonal flow structures. This gives us the opportunity to measure physical properties such as size and lifetime independent of the simulated domain. Further, we investigate properties of the zonal flows in radially and azimuthally stretched boxes. We alter the radial and azimuthal domain up to  $\sim 20$  gas pressure scale heights.

Additionally, we study the behavior of dust in zonal flows. Whipple (1972) was the first to suggest that axisymmetric pressure bumps can trap gas. Pinilla et al. (2012) invoked zonal flows as a possibility to explain the submillimeter and millimeter-sized particles observed in protoplanetary disks. They used artificial static density bumps introduced as sinusoidal density perturbations with different amplitudes (e.g.,  $A = 0.1$  and  $A = 0.3$ ) and different wavelengths ( $L = 0.3 \dots 3H$ ). They found that a 30% density perturbation (with  $L = 1H$ ) is necessary to stop the drift of the dust grains. The present work is the first three-dimensional MHD study that combines zonal flows and the reaction of dust particles on them.

Our paper is organized as follows. In Section 2 we discuss the setup of the simulations in this paper. In Section 3 we study the zonal flow properties and their dependency on the physical box size. The behavior of dust particles in zonal flows is described in Section 4. A discussion and conclusions follows in Section 5 and Section 6 provides a summary and an outlook.

## 2. SIMULATION SETUP

We use the Pencil Code,<sup>1</sup> a sixth-order spatial and third-order temporal finite difference code, for our simulations. We simulated the standard ideal MHD equations in a local shearing box with vertical stratification. The simulation boxes are centered at an arbitrary distance  $r$  to the star. The radial direction is denoted by  $x$ , the azimuthal direction by  $y$ , and the vertical direction by  $z$ . The Keplerian frequency is  $\Omega$ . We include dust particle dynamics, without back-reaction to the gas and without self-gravity.

### 2.1. Gas Dynamics

The gas velocity  $\mathbf{u}$  relative to the Keplerian shear is evolved via the equation of motion

$$\begin{aligned} \frac{\partial \mathbf{u}}{\partial t} + (\mathbf{u} \cdot \nabla) \mathbf{u} + u_y^{(0)} \frac{\partial \mathbf{u}}{\partial y} = \\ 2 \Omega u_y \hat{x} - \frac{1}{2} \Omega u_x \hat{y} + \Omega^2 z \hat{z} \\ + \frac{1}{\rho} \mathbf{J} \times \mathbf{B} - \frac{1}{\rho} \nabla P + \mathbf{f}_\nu(\mathbf{u}, \rho). \end{aligned} \quad (1)$$

On the left-hand side of the equation, the second and third terms are the advection terms by the perturbed

velocity and by shear flow, respectively. The right-hand side contains the Coriolis force, the vertical component of the stellar gravity, the Lorentz force, the pressure gradient, and the viscosity term. Here,  $u_y^{(0)} = -(3/2)\Omega x$  is the Keplerian orbital velocity. The magnetic field  $\mathbf{B}$  as well as the current density  $\mathbf{J}$  are calculated from the vector potential  $\mathbf{A}$  using  $\mathbf{B} = \nabla \times \mathbf{A}$  and  $\mathbf{J} = \mu_0^{-1} \nabla \times (\nabla \times \mathbf{A})$ , respectively. Here,  $\mu_0$  is the vacuum permeability. The viscosity term  $\mathbf{f}_\nu$  is explained in Section 2.2.1.

We evolve the magnetic potential with the uncurled induction equation

$$\frac{\partial \mathbf{A}}{\partial t} + u_y^{(0)} \frac{\partial \mathbf{A}}{\partial y} = \mathbf{u} \times \mathbf{B} + \frac{3}{2} \Omega A_y \hat{x} + \mathbf{f}_\eta(\mathbf{A}). \quad (2)$$

The terms on the right-hand side express the electromotive force, the stretching (creation of azimuthal magnetic field from radial field) by Keplerian shear and the resistivity  $\mathbf{f}_\eta$  (see Section 2.2.2).

The gas density is evolved with the continuity equation

$$\frac{\partial \rho}{\partial t} + (\mathbf{u} \cdot \nabla) \rho + u_y^{(0)} \frac{\partial \rho}{\partial y} = -\rho \nabla \cdot \mathbf{u} + f_D(\rho), \quad (3)$$

where the last term on the right-hand side describes mass diffusion (see Section 2.2.3). We use an isothermal equation of state  $P = c_s^2 \rho$ , where the speed of sound is  $c_s = H\Omega$ ;  $H$  is the gas pressure scale height.

### 2.2. Dissipation

Maxwell and Reynolds stresses as well as the MRI release kinetic and magnetic energy at large scales. This energy cascades down to small scales. Since numerical simulations have a finite resolution, this small-scale energy needs to be dissipated. We use numerical dissipation in the form of hyper- and shock viscosity (Section 2.2.1), hyper-resistivity (Section 2.2.2), and hyper- and shock diffusion (Section 2.2.3).

#### 2.2.1. Viscosity

The viscosity term  $\mathbf{f}_\nu$  in Equation (1) is expressed by

$$\begin{aligned} \mathbf{f}_\nu = \nu_3 \left[ \nabla^6 \mathbf{u} + \left( \mathbf{S}^{(3)} \cdot \nabla \ln \rho \right) \right] \\ + \nu_{\text{sh}} \left[ \nabla \nabla \cdot \mathbf{u} + (\nabla \cdot \mathbf{u}) (\nabla \cdot \ln \rho) \right] \\ + (\nabla \nu_{\text{sh}}) \nabla \cdot \mathbf{u}. \end{aligned} \quad (4)$$

We restricted our models to hyper- ( $\nu_3$ ) and shock ( $\nu_{\text{sh}}$ ) viscosity. Thus, the regular Navier-Stokes viscosity term is neglected. The third-order rate-of-strain tensor  $\mathbf{S}^{(3)}$  is defined by

$$S_{ij}^{(3)} = \frac{\partial^5 u_i}{\partial x_j^5}. \quad (5)$$

The high-order Laplacian  $\nabla^6$  in Equation (4) is expanded as  $\nabla^6 = \partial^6 / \partial x^6 + \partial^6 / \partial y^6 + \partial^6 / \partial z^6$ . Furthermore, the shock viscosity is expressed by

$$\nu_{\text{sh}} = c_{\text{sh}} \langle \max[-\nabla \cdot \mathbf{u}]_+ \rangle \min(\delta x, \delta y, \delta z)^2. \quad (6)$$

In the fashion of von Neumann & Richtmyer (1950) it is proportional to positive<sup>2</sup> flow convergence. We take the

<sup>1</sup> Details on the Pencil Code and download information can be found at <http://www.nordita.org/software/pencil-code/>.

<sup>2</sup> Symbolized by the plus sign in Equation (6). We only apply shock viscosity where the velocity flow is converging.

maximum over five zones, and smoothed it to the second order. As suggested by von Neumann & Richtmyer (1950), we set the shock viscosity coefficient to  $c_{sh} = 1.0$  to dissipate energy in shocks at high  $z$  above the mid-plane of the disk.

### 2.2.2. Resistivity

The effects of resistivity are captured by the term

$$\mathbf{f}_\eta = \eta_3 \nabla^6 \mathbf{A}, \quad (7)$$

where  $\eta_3$  is the hyper-resistivity.

### 2.2.3. Diffusion

Mass diffusion is computed with

$$f_D = D_3 \nabla^6 \rho + D_{sh} \nabla^2 \rho + \nabla D_{sh} \cdot \nabla \rho, \quad (8)$$

where  $D_3$  is the hyper-diffusion parameter and  $D_{sh}$  is expanded as in Equation (6).

### 2.3. Dust Dynamics

Dust particles are simulated as individual super-particles  $i$  with position  $\mathbf{x}_i$  and velocity  $\mathbf{v}_i$ . Each super-particle position is evolved with

$$\frac{d\mathbf{x}^{(i)}}{dt} = \mathbf{v}^{(i)} + u_y^{(0)} \hat{\mathbf{y}}. \quad (9)$$

The change of velocity for each particle is evolved through

$$\begin{aligned} \frac{d\mathbf{v}^{(i)}}{dt} = & 2\Omega v_y^{(i)} \hat{\mathbf{x}} - \frac{1}{2}\Omega v_x^{(i)} \hat{\mathbf{y}} - \Omega^2 z \hat{\mathbf{z}} \\ & - \frac{1}{\tau_f} [\mathbf{v}^{(i)} - \mathbf{u}(\mathbf{x}^{(i)})], \end{aligned} \quad (10)$$

where the first and second terms are due to the Coriolis force. The third term corresponds to the vertical gravity of the star. Particles only feel the gas drag (the last term in Equation (10)) of nearby cells, but are not subjected to pressure or Lorentz forces.  $\tau_f$  denotes the friction time, a measure for the size of the particles.

### 2.4. Boundary Conditions

For our simulations, we use shearing box boundary conditions in radial (shear-periodic) and azimuthal (periodic) directions. In the vertical direction we also use periodic boundary conditions. Although periodic boundary conditions in vertical direction are not physical, these boundary conditions conserve the average flux of the magnetic field. Simulations with outflow boundaries (not included in this paper) showed no considerable mass flux across the vertical boundary and did not change the average properties of the zonal flow.

### 2.5. Dimensions

We use the dimensionless unit system  $c_s = \Omega = \mu_0 = \rho_0 = 1$ . Velocity is measured in units of the local sound speed  $c_s$ . Gas velocities are always denoted by  $\mathbf{u}$  whereas particle velocities are always denoted by  $\mathbf{v}$ . All velocities are differences to the Keplerian orbital velocity  $\mathbf{v}_K = (0, u_y^{(0)}, 0)$ , where  $u_y^{(0)} = -(3/2)\Omega x$ . Time is measured in units of the local orbital time  $T_{orb} = 2\pi\Omega^{-1}$ . Length

measures are in units of the pressure scale height  $H = c_s\Omega^{-1}$ . Density is stated in units of the initial mid-plane gas density  $\rho_0$ . Magnetic field strength is measured in units of  $c_s(\mu_0\rho_0)^{-1}$ . Energy and stress are in units of the mean thermal pressure in the box  $\langle P \rangle = c_s^2 \langle \rho \rangle$ .

Since our simulations are dimensionless, they can be placed at any distance  $r$  to the star. Only by defining a global pressure gradient  $\partial P_{global}/\partial r$ , which balances the Coriolis force in

$$\frac{1}{\rho} \frac{\partial P_{global}}{\partial r} = 2\Omega \Delta v, \quad (11)$$

we restrict our simulations to a specific distance to the star where the chosen pressure gradient applies. The parameter  $\Delta v = u_y^{(0)} - u_y$  is the difference to the azimuthal Keplerian velocity. We fix  $\Delta v = 0.05c_s$  (see also Section 2.6). Numerically, the global pressure gradient acts as an external force on gas and dust.

### 2.6. Initial Conditions

The gas density is set to an isothermal hydrostatic equilibrium  $\rho(z) = \rho_0 \exp(-z^2/2H^2)$ . We start with random noise fluctuations in the gas velocity with  $\delta\mathbf{u} = 10^{-3}c_s$ . The azimuthal component of the magnetic vector potential is initialized with  $A_y = A_0 \cos(k_x x) \cos(k_y y) \cos(k_z z)$  where throughout  $k_x = k_y = k_z = 4.76H^{-1}$  and  $A_0 = 0.04c_s(\mu_0\rho_0)^{-1}$ .

Particles are released after the gas turbulence is saturated. We measured this to be after  $20T_{orb}$  for the largest runs. For convenience, we used the same saturation time for all our simulations. Particles have a Stokes number of  $St = \tau_f\Omega = 1$ , unless otherwise stated. The initial particle distribution is Gaussian in  $z$  and uniform in  $x$  and  $y$ . The particle velocity is initialized with the stationary solution (Nakagawa et al. 1986) for the radial and azimuthal velocity

$$\begin{aligned} \frac{v_x}{c_s} = & -\frac{2\Delta v}{\tau_f\Omega + (\tau_f\Omega)^{-1}} \\ \frac{v_y}{c_s} = & -\frac{\Delta v}{1 + (\tau_f\Omega)^2}. \end{aligned} \quad (12)$$

We get  $\Delta v$  from the solution of Equation (11)

$$\frac{\Delta v}{c_s} = -\frac{1}{2} \left( \frac{H}{r} \right)^2 \frac{\partial \ln P}{\partial \ln r}. \quad (13)$$

We initialized  $\Delta v = 0.05c_s$  for our simulations.

### 2.7. Simulation Parameters

The parameter space covered by our simulations is summarized in Figure 1. The vertical extent is always set to  $L_z = 2.64H$ .<sup>3</sup> One simulation set (A) covers the boxes with a squared base, i.e., radial and azimuthal extent are kept the same:  $L_x = L_y = \{1.32, 2.64, 5.28, 10.56, 21.12\}H$ . These are marked with blue boxes in Figure 1 and are called runs *S*, *M*, *L*, *XL*, and *XXL*. The deviation to the global density profile in the largest box

<sup>3</sup>  $L = 1.32$  has been chosen as the basic box size, because  $L_x = 1.32$  approximately marks the transition from subsonic to supersonic Keplerian shear flow (Johansen et al. 2009a).

**Table 1**  
Run Parameters

Simulation Set (1)	Run (2)	$L_x \times L_y \times L_z$ (3)	$N_x \times N_y \times N_z$ (4)	$\nu_3 = \eta_3 = D_3$ (5)	$n_{\text{particles}}$ (6)	St (7)	Shear (8)	$\Delta t$ (9)
A	S	$1.32 \times 1.32 \times 2.64$	$36 \times 36 \times 72$	$4.0 \times 10^{-10}$	62,500	1.0	FDA	121
A,B,C	M	$2.64 \times 2.64 \times 2.64$	$72 \times 72 \times 72$	$4.0 \times 10^{-10}$	250,000	1.0	FDA	121
A,E	L	$5.28 \times 5.28 \times 2.64$	$144 \times 144 \times 72$	$4.0 \times 10^{-10}$	1,000,000	1.0	FDA	121
A,E	XL	$10.56 \times 10.56 \times 2.64$	$288 \times 288 \times 72$	$4.0 \times 10^{-10}$	4,000,000	1.0	FDA	121
A	XXL	$21.12 \times 21.12 \times 2.64$	$576 \times 576 \times 72$	$4.0 \times 10^{-10}$	4,000,000	1.0	FDA	121
B	x-S	$1.32 \times 2.64 \times 2.64$	$36 \times 72 \times 72$	$4.0 \times 10^{-10}$	125,000	1.0	FDA	121
B	x-L	$5.28 \times 2.64 \times 2.64$	$144 \times 72 \times 72$	$4.0 \times 10^{-10}$	500,000	1.0	FDA	121
B	x-XL	$10.56 \times 2.64 \times 2.64$	$288 \times 72 \times 72$	$4.0 \times 10^{-10}$	1,000,000	1.0	FDA	121
C	y-S	$2.64 \times 1.32 \times 2.64$	$72 \times 36 \times 72$	$4.0 \times 10^{-10}$	125,000	1.0	FDA	121
C	y-L	$2.64 \times 5.28 \times 2.64$	$72 \times 144 \times 72$	$4.0 \times 10^{-10}$	500,000	1.0	FDA	121
C	y-XL	$2.64 \times 10.56 \times 2.64$	$72 \times 288 \times 72$	$4.0 \times 10^{-10}$	1,000,000	1.0	FDA	121
D	LspecMR	$5.28 \times 5.28 \times 2.64$	$144 \times 144 \times 72$	$4.0 \times 10^{-10}$	1,200,000	0.01 ... 100	FDA	121
D	LspecHR	$5.28 \times 5.28 \times 2.64$	$256 \times 256 \times 128$	$2.0 \times 10^{-11}$	120,000,000	0.01 ... 100	FDA	121
D	LspecMRs	$5.28 \times 5.28 \times 2.64$	$144 \times 144 \times 72$	$4.0 \times 10^{-10}$	14,000,000	0.01 ... 1.0	FDA	121
D	MspecMRb	$2.64 \times 2.64 \times 2.64$	$72 \times 72 \times 72$	$4.0 \times 10^{-10}$	6,000,000	1.0 ... 100	FDA	223
E	L_SAFI	$5.28 \times 5.28 \times 2.64$	$144 \times 144 \times 72$	$4.0 \times 10^{-10}$	1,000,000	1.0	SAFI	121
E	XL_SAFI	$10.56 \times 10.56 \times 2.64$	$288 \times 288 \times 72$	$4.0 \times 10^{-10}$	4,000,000	1.0	SAFI	121

Notes. Column 1: simulation set. Column 2: name of run. Column 3: box size in units of pressure scale heights. Column 4: grid resolution. Column 5: dissipation coefficients. Column 6: number of particles in simulation. Column 7: Stokes number  $\text{St} = \tau_f \Omega$ . Column 8: shear advection scheme. Column 9: total run time in orbits  $T_{\text{orb}}$ .

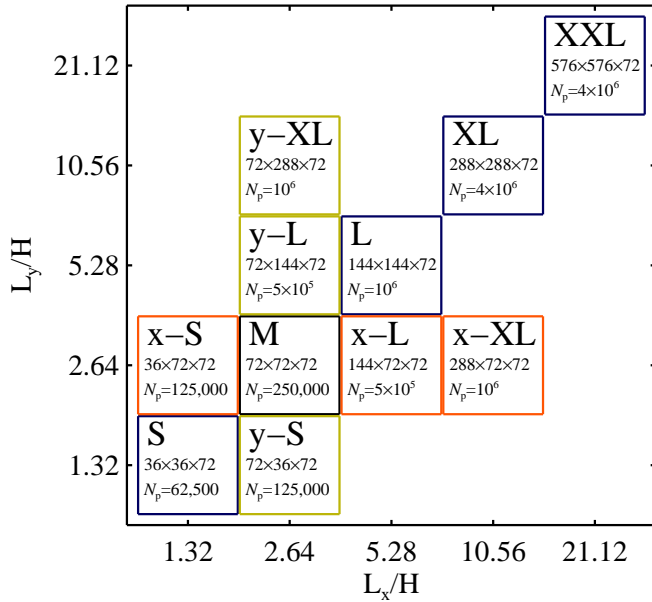


**Figure 1.** Parameter space of radial and azimuthal box sizes that was simulated for this paper. Every simulation has a vertical extent of  $2.64H$ . The first line in each box states the name of the run, the second line the number of grid cells used, and the third line gives the number of simulated super-particles. More details on all simulations are found in Table 1.

can be quite severe at the inner and outer boundary of the largest simulation. Thus, the results from run *XXL* have to be treated with caution. Another set of simulations (*B*) varies the radial size of the box,  $L_x = \{1.32, 2.64, 5.28, 10.56\}H$ , with constant box size in azimuthal direction,  $L_y = 2.64H$ . This set is marked red in Figure 1 and includes runs *x-S*, *M*, *x-L*, and *x-XL*. The third set of simulations (*C*) varies the azimuthal extent,  $L_y = \{1.32, 2.64, 5.28, 10.56\}H$ , while the radial extent is kept constant,  $L_x = 2.64H$ . This set includes runs *y-S*, *M*, *y-L*, and *y-XL* (marked

yellow in Figure 1). All simulations are stratified and have dust particles with different couplings to the gas. The simulations displayed in Figure 1 have particles with a Stokes number of  $\text{St} = 1$ .

Details on run parameters of those and six more simulations are found in Table 1. The first set of simulations (*A*, *B*, and *C*) in Table 1 are the simulations with medium resolution, i.e., 36 grid cells<sup>4</sup> per 1.32 pressure scale heights. Simulation set *D* was carried out to investigate the behavior of different particle sizes in the presence of zonal flows. Run *LspecMR* is very much like run *L*, but with 12 different particle Stokes numbers. The run *LspecHR* has a resolution of 64 grid cells per  $1.32H$ . Runs *LspecMR* and *LspecHR* have 12 different particle species, with Stokes numbers of  $\text{St} = 0.01 \dots 100.0$ . The runs *LspecMRs* and *MspecMRb* have particles with Stokes numbers of  $\text{St} = 0.01 \dots 1.0$  and  $\text{St} = 1.0 \dots 100.0$ , respectively. These two simulations were carried out to study particle behavior with more particles per grid cell<sup>5</sup> at medium resolution. The corresponding sizes for different protoplanetary disk models are found in Section 5.2.

Simulation set *E* is a comparison of runs *L* and *XL* to the same runs (*L\_SAFI* and *XL\_SAFI*) with the Shear Advection by Fourier Interpolation (SAFI) scheme. Here, all variables  $q(x, y, z)$  are transformed into Fourier space in the *y*-direction to get  $\hat{q}(x, k_y, z)$ . Then each Fourier mode is multiplied by  $\exp[ik_y u_y^{(0)}(x)\delta t]$  to shift by  $u_y^{(0)}(x)\delta t$  in real space and is inverse Fourier transformed to real space. This method reduces the advection error to the standard Finite Difference Advection (FDA) scheme in the Pencil Code (more details on FDA and SAFI are found in Johansen et al. 2009a).

<sup>4</sup> We chose 36 grid cells instead of the usual 32 grid cells. That choice was done due to the architecture (12 CPUs per node) of the used cluster, THEO in the MPG computing center in Garching.

<sup>5</sup>  $\sim 9$  and  $\sim 16$  particles per grid cell for runs *LspecMRs* and *MspecMRb* compared to  $\sim 0.8$  particles per grid cell for run *LspecMR*.



**Table 2**  
Turbulence Properties

Run (1)	$\langle \frac{1}{2} u_x^2 \rangle$ (2)	$\langle \frac{1}{2} u_y^2 \rangle$ (3)	$\langle \frac{1}{2} u_z^2 \rangle$ (4)	$\langle \frac{1}{2} B_x^2 \rangle$ (5)	$\langle \frac{1}{2} B_y^2 \rangle$ (6)	$\langle \frac{1}{2} B_z^2 \rangle$ (7)	$\langle \rho u_x u_y \rangle$ (8)	$\langle -B_x B_y \rangle$ (9)	$\alpha$ (10)
S	$2.1 \times 10^{-3}$	$3.3 \times 10^{-3}$	$1.5 \times 10^{-3}$	$8.8 \times 10^{-4}$	$6.4 \times 10^{-3}$	$3.5 \times 10^{-4}$	$7.7 \times 10^{-4}$	$3.4 \times 10^{-3}$	$2.8 \times 10^{-3}$
M	$3.9 \times 10^{-3}$	$5.2 \times 10^{-3}$	$2.2 \times 10^{-3}$	$1.9 \times 10^{-3}$	$1.2 \times 10^{-2}$	$7.6 \times 10^{-4}$	$1.6 \times 10^{-3}$	$6.6 \times 10^{-3}$	$5.5 \times 10^{-3}$
L	$5.0 \times 10^{-3}$	$5.6 \times 10^{-3}$	$2.3 \times 10^{-3}$	$2.0 \times 10^{-3}$	$1.3 \times 10^{-2}$	$8.0 \times 10^{-4}$	$1.9 \times 10^{-3}$	$6.9 \times 10^{-3}$	$5.9 \times 10^{-3}$
XL	$5.2 \times 10^{-3}$	$5.0 \times 10^{-3}$	$2.1 \times 10^{-3}$	$1.7 \times 10^{-3}$	$1.1 \times 10^{-2}$	$6.7 \times 10^{-4}$	$1.8 \times 10^{-3}$	$6.1 \times 10^{-3}$	$5.2 \times 10^{-3}$
XXL	$5.1 \times 10^{-3}$	$4.6 \times 10^{-3}$	$2.0 \times 10^{-3}$	$1.6 \times 10^{-3}$	$1.0 \times 10^{-2}$	$6.2 \times 10^{-4}$	$1.7 \times 10^{-3}$	$5.7 \times 10^{-3}$	$4.9 \times 10^{-3}$
x-S	$4.0 \times 10^{-3}$	$5.2 \times 10^{-3}$	$2.4 \times 10^{-3}$	$2.0 \times 10^{-3}$	$1.3 \times 10^{-2}$	$8.4 \times 10^{-4}$	$1.7 \times 10^{-3}$	$7.0 \times 10^{-3}$	$5.8 \times 10^{-3}$
x-L	$3.8 \times 10^{-3}$	$5.2 \times 10^{-3}$	$2.1 \times 10^{-3}$	$1.7 \times 10^{-3}$	$1.1 \times 10^{-2}$	$6.9 \times 10^{-4}$	$1.5 \times 10^{-3}$	$6.1 \times 10^{-3}$	$5.1 \times 10^{-3}$
x-XL	$3.8 \times 10^{-3}$	$5.0 \times 10^{-3}$	$2.2 \times 10^{-3}$	$1.8 \times 10^{-3}$	$1.2 \times 10^{-2}$	$7.1 \times 10^{-4}$	$1.5 \times 10^{-3}$	$6.2 \times 10^{-3}$	$5.2 \times 10^{-3}$
y-S	$2.3 \times 10^{-3}$	$3.7 \times 10^{-3}$	$1.6 \times 10^{-3}$	$1.0 \times 10^{-3}$	$7.1 \times 10^{-3}$	$4.1 \times 10^{-4}$	$8.6 \times 10^{-4}$	$3.8 \times 10^{-3}$	$3.1 \times 10^{-3}$
y-L	$5.2 \times 10^{-3}$	$5.7 \times 10^{-3}$	$2.5 \times 10^{-3}$	$2.2 \times 10^{-3}$	$1.4 \times 10^{-2}$	$8.8 \times 10^{-4}$	$2.0 \times 10^{-3}$	$7.5 \times 10^{-3}$	$6.3 \times 10^{-3}$
y-XL	$5.4 \times 10^{-3}$	$5.0 \times 10^{-3}$	$2.2 \times 10^{-3}$	$1.8 \times 10^{-3}$	$1.2 \times 10^{-2}$	$7.2 \times 10^{-4}$	$1.9 \times 10^{-3}$	$6.4 \times 10^{-3}$	$5.6 \times 10^{-3}$
LspecMR	$4.8 \times 10^{-3}$	$5.3 \times 10^{-3}$	$2.2 \times 10^{-3}$	$1.9 \times 10^{-3}$	$1.2 \times 10^{-2}$	$7.5 \times 10^{-4}$	$1.8 \times 10^{-3}$	$6.6 \times 10^{-3}$	$5.6 \times 10^{-3}$
LspecHR	$3.0 \times 10^{-3}$	$4.2 \times 10^{-3}$	$1.4 \times 10^{-3}$	$1.3 \times 10^{-3}$	$7.5 \times 10^{-3}$	$5.4 \times 10^{-4}$	$1.0 \times 10^{-3}$	$4.2 \times 10^{-3}$	$3.5 \times 10^{-3}$
LspecMRs	$5.3 \times 10^{-3}$	$6.2 \times 10^{-3}$	$2.5 \times 10^{-3}$	$2.2 \times 10^{-3}$	$1.4 \times 10^{-2}$	$9.2 \times 10^{-4}$	$2.1 \times 10^{-3}$	$7.7 \times 10^{-3}$	$6.5 \times 10^{-3}$
MspecMRb	$4.3 \times 10^{-3}$	$5.7 \times 10^{-3}$	$2.5 \times 10^{-3}$	$2.1 \times 10^{-3}$	$1.4 \times 10^{-2}$	$8.7 \times 10^{-4}$	$1.8 \times 10^{-3}$	$7.2 \times 10^{-3}$	$6.0 \times 10^{-3}$
LSAFI	$5.1 \times 10^{-3}$	$5.8 \times 10^{-3}$	$2.4 \times 10^{-3}$	$2.1 \times 10^{-3}$	$1.3 \times 10^{-2}$	$8.4 \times 10^{-4}$	$2.0 \times 10^{-3}$	$7.2 \times 10^{-3}$	$6.1 \times 10^{-3}$
XLSAFI	$5.4 \times 10^{-3}$	$5.3 \times 10^{-3}$	$2.2 \times 10^{-3}$	$1.8 \times 10^{-3}$	$1.2 \times 10^{-2}$	$7.3 \times 10^{-4}$	$1.9 \times 10^{-3}$	$6.5 \times 10^{-3}$	$5.6 \times 10^{-3}$

Notes. Column 1: name of run. Columns 2-4: kinetic energy. Columns 5-7: magnetic energy. Column 8: Reynolds stress. Column 9: Maxwell stress. Column 10:  $\alpha$ -value, following Equation (14). Stresses and energies have been normalized to the mean thermal pressure in the box,  $\langle P \rangle = c_s^2 \langle \rho \rangle$ .

Every simulation is run for 121 local orbits  $T_{\text{orb}} = 2\pi\Omega^{-1}$ , except for *LspecMRb* which runs for  $223T_{\text{orb}}$  in order to follow the evolution of the slowly settling large particles. After  $20T_{\text{orb}}$ , when the initial conditions are sufficiently forgotten and the turbulence saturated, the particles are started.

### 3. ZONAL FLOW PROPERTIES

Turbulence properties are summarized in Table 2. The kinetic and magnetic energy as well as the Reynolds and Maxwell stress almost doubles when increasing the box size from  $(1.32H)^2 \times 2.64H$  (run *S*) to  $(2.64H)^3$  (run *M*). Further increasing the box size does not change the resulting energies and stresses by much. The radially short box of run *x-S* with  $1.32H \times (2.64H)^2$  has similar results on these values. However, the azimuthally short box of run *y-S* has turbulent energies and stresses comparable to run *S*. These measurements show that the turbulence parameters are saturated for boxes with an azimuthal extent of at least  $2.64H$ . This confirms the results from Fromang & Stone (2009) who found that the turbulence properties do not change when the box size is increased radially, if the azimuthal dimension is large enough. The  $\alpha$ -value (Shakura & Sunyaev 1973) in Column 10 in Table 2 is calculated via

$$\alpha = \frac{2}{3} \frac{\langle \rho u_x u_y \rangle - \langle B_x B_y \rangle}{\langle P \rangle}, \quad (14)$$

where  $\langle P \rangle = c_s^2 \langle \rho \rangle$ . The factor of  $2/3$  originates from the shear parameter  $q = -d \ln \Omega / d \ln R$ . We use  $q = 3/2$ , appropriate for a Keplerian disk. For further details see Brandenburg et al. (1995, page 748). The Maxwell stress is around three times higher than the Reynolds stress and thus dominates the  $\alpha$ -value.

In order to verify that our numerical resolution is sufficient, we examined the quality factor as described in

Simon et al. (2012):

$$Q_j = \frac{2\pi |v_{a,j}|}{\Omega \Delta x_j}, \quad (15)$$

where the Alfvén speed is defined as  $|v_{a,j}|^2 = \langle B_j \rangle^2 / \langle \rho \rangle$ . The notation  $\langle x \rangle$  denotes volume averaging,  $\bar{x}$  shows a time average. Sorathia et al. (2012) show that  $Q_z \gtrsim 10 - 15$  for poorly resolved azimuthal quality factors ( $Q_y \sim 10$ ) is required to resolve the MRI. Larger values of the azimuthal quality factor ( $Q_y \gtrsim 25$ ) allow for lower vertical quality factors. The azimuthal component of the magnetic field is very well resolved ( $Q_y \gtrsim 25$ ) for all simulations, but runs *S* and *y-S*. The vertical component has values between 6 and 8. We thus conclude that all simulations, but runs *S* and *y-S* have sufficient resolution for the MRI.

In Figure 2 a snapshot of the runs *y-XL*, *XL*, *M*, and *x-XL* are shown in scale, giving a real size comparison of high- and low-pressure regions. The large-scale sinusoidal form of the dominant mode is observable in these plots. The higher modes are much shorter lived and seem to be non-axisymmetric density waves affected by the shear (Heinemann & Papaloizou 2009). The amplitudes of the pressure differences are higher in azimuthally large boxes. Only the axisymmetric density waves are long-lived and strong enough to make up a significant contribution to the pressure bump structure in an azimuthal as well as a temporal average over some local orbits. The azimuthal average of Figure 2 is seen in Figure 3. Here, the axisymmetric structure is clearly visible and a strong correlation between the particle location and a positive radial gradient of the gas density is seen. The black dots in Figures 2 and 3 show the radial and azimuthal position of every 100th particle. The particles are trapped by the axisymmetric pressure bumps. Also, the shapes of spiral density waves (Heinemann & Papaloizou 2009) can be seen in the structures. The particle distribution with respect to the gas flow will be discussed in more

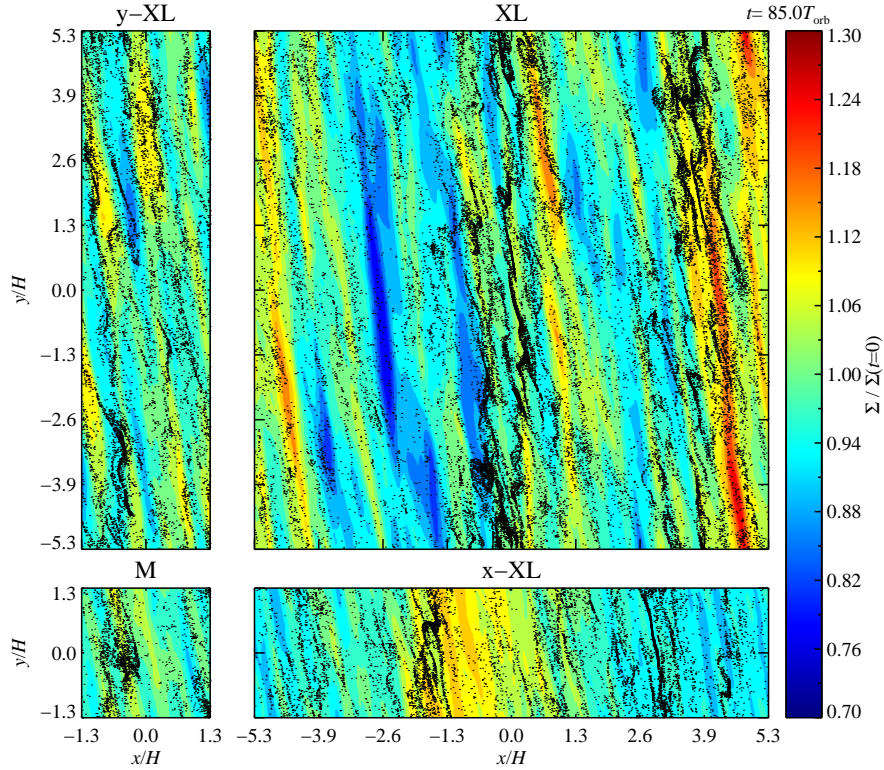


**Figure 2.** Collage of four gas surface density representations of the runs *y-XL*, *XL*, *M*, and *x-XL*. Each snapshot was taken after  $85T_{\text{orb}}$ . These plots show that gas overdensities are most pronounced in the largest box. The non-axisymmetric structures have very short lifetimes; less than a tenth of an orbit. The pressure bump structures are more visible when the density is averaged over the azimuthal direction (Figure 3). The black dots represent the position of every 100th particle, integrated in vertical direction. The particles are trapped both in axisymmetric pressure bumps and in spiral density waves as described in Heinemann & Papaloizou (2009).

detail in Section 4.

All of our simulations show signs of zonal flows. Strength and lifetime of the zonal flows and the associated pressure bumps differ very much with the physical box size. Space-time plots of all different simulation sizes are shown in Figure 4 and the upper left panel of Figure 5. The pressure bumps are generally more pronounced in simulations with a larger radial extent. Simulation set *A* strictly follows this general trend. Pressure bump features grow in strength and lifetime with the physical box size, always staying at the largest radial scale. This rule applies to all but the largest runs *XL*, *x-XL*, and *XXL*. There, instead of the formerly predominant  $k_x = 1$  ( $\omega_x = 2\pi k_x / L_x$  in Fourier mode  $\sin(\omega_x x)$ ) mode, the mode  $k_x = 2$  (higher modes for run *XXL*) is occupied by the pressure bumps. In simulation set *B*, the strength and size of the pressure bumps converges for simulations with a radial extent larger than  $5.28H$ . The lifetime of the pressure bumps even decreases for the largest simulation in this set. Simulation set *C* is qualitatively different from the other simulation sets. Strength, size, and lifetime of the pressure bumps seem to be inversely proportional to the azimuthal extent of the box, when the vertical and radial box sizes are kept constant. This effect was already seen in, e.g., Simon et al. (2012) and Flock et al. (2012). Both groups show that the magnetic field consists of two components: a local turbulent component that is responsible for the zonal flows and a global azimuthal component. Since the total energy stays approximately constant, the local component gets weaker and consequently zonal flows as well as axisym-

metric pressure bumps get weaker too.

Figure 5 additionally shows space-time plots of the azimuthal gas velocity and the radial gradients of gas density and azimuthal gas velocity of run *XXL*. In the right panels, the position of the highest dust density are shown as dots. Particles get clearly slowed by the maxima of the azimuthal gas velocity, i.e., the large-scale maxima of the pressure gradients. The velocity has large-scale structures that are very similar to those of the density gradient, as expected in geostrophic balance. Thus, the structure of the velocity gradient can be approximated as the large-scale structure of the second derivative of the gas density. It is shown in the lower right panel that the particles get stopped at the minima of the radial derivative of the azimuthal gas velocity (and thus at minima of the second derivative of the gas density) as analytically predicted (see, e.g., Klahr & Lin 2001).

We calculated the correlation time of the pressure bumps and the zonal flows in the same way as it was calculated in Johansen et al. (2009a). We use the density  $\rho$ , averaged over azimuthal and vertical directions, at a given time  $t$ . Then, we average over each point in radial direction the time it takes for the density at each point to change by a value corresponding to the standard deviation of the gas density. These measurements are taken for every local orbit. The measurements are averaged over the time between saturation of the turbulence and a time when the correlation does not extend the correlation time to the final time of the simulation. Finally, the averages are multiplied by two, in order to cover the full temporal extent of the correlated structures. The

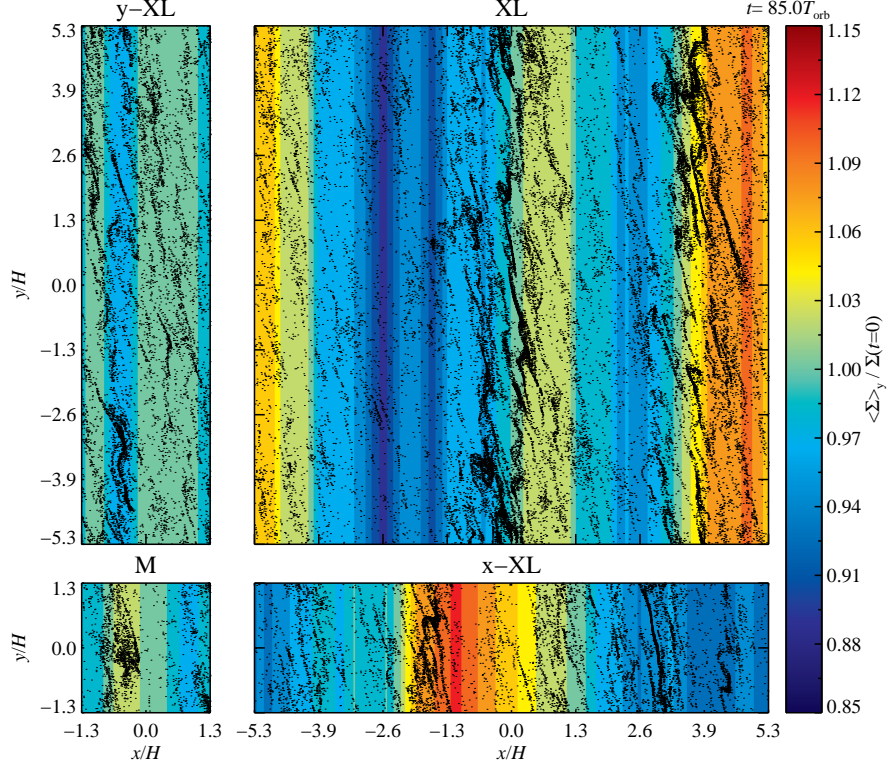


**Figure 3.** Surface density distribution of Figure 2, averaged in azimuthal direction and averaged over the mean surface density. This reveals axisymmetric pressure bumps and valleys. Particles are trapped on the inner side of the density maxima, at places with a positive density gradient to overcome the negative global pressure gradient. These pressure bumps are stable for many orbits (compare Figures 4 and 5).

correlation times measured in this fashion are in good agreement with the lifetime of the overdensities that is seen in Figures 4 and 5. However, a change of position of the structures, as seen in run *XL* (check Figure 4), is not accounted for. Thus, correlation times are more likely to be underestimated than overestimated. Also, we cannot be entirely sure whether this behavior is really drift or structure decay and reformation.

The results of the correlation time determination are shown in Table 3 and in the upper panel of Figure 6. For the diagonal simulation set, (A), the correlation time increases with box size. It seems to saturate toward the largest box size. The trend to longer correlation times is also evident for simulation set *B*. Here only run *x-XL* has a shorter correlation time than expected. This might be an effect of the strongly stretched simulation box. The correlation time decreases slightly with an increasing azimuthal box size in simulation set *C* (not shown in the figure). The lower panel in Figure 6 shows a measurement for the physical size of the zonal flow features. We Fourier-transformed the vertically and azimuthally averaged gas density and azimuthal gas velocity for each time step and averaged the amplitudes of the first four modes over the time of 20...120 local orbits. The length was normalized for the size of the simulation box, to get the physical size of the modes by  $\lambda_x = L_x/k_x$  with the wave number  $k_x$ . The turbulence is always strongest at the largest modes for simulations with  $L_x \lesssim 5H$ . The highest amplitude for both quantities in the largest simulation domain is found between  $5H$  and  $7H$  (up to  $10H$  for  $\hat{\rho}$ ). These measurements are also found in Table 3.

The runs *L-SAFI* and *XL-SAFI* were carried out to compare the turbulence and zonal flow parameters with the runs *L* and *XL*. They were run to check that zonal flows are no effects from the shear advection scheme that was used in the Pencil Code. Comparing the values in Tables 2 and 3 shows that there is little change in the measured properties of the zonal flows and the associated pressure bumps. However, the computation time increases if one uses the SAFI scheme. Thus, this scheme was only used to confirm our results.

#### 4. PARTICLE BEHAVIOR IN ZONAL FLOWS

Particle accumulations and planetesimal formation can occur in clumps and filaments of the overdensities in the dust. In our simulations, we do not include gravitational interaction between the particles. Thus, we only study the passively developed overdensities of the dust to see when and whether overdensities sufficient for the streaming instability can be reached. By not having explicit feedback one can retroactively study the concentration factor for various initial dust-to-gas ratios. Simulations including feedback will have to be done in future studies. Figure 2 shows the position of every 100th particle in selected simulations. These plots clearly show the trend for particles to accumulate in the downstream of high-pressure regions. Particles are pulled toward pressure gradient maxima (Klahr & Lin 2001). In the upper right panel in Figure 2, a snapshot of run *XL* after 85 local orbits is shown. The particles clump up at positions just left of the maxima in the  $k_x = 1$  of the gas density; these are the locations of positive zonal flows,



**Table 3**  
Zonal Flow Properties

Run (1)	$\rho_{\text{rms}}$ (2)	$ \hat{\rho}(k_x = 1) $ (3)	$ \hat{\rho}(k_x = 2) $ (4)	$ \hat{\rho}(k_x = 3) $ (5)	$ \hat{u}_y(k_x = 1) $ (6)	$ \hat{u}_y(k_x = 2) $ (7)	$ \hat{u}_y(k_x = 3) $ (8)	$\tau_{\text{corr}}$ (9)
S	$6.1 \times 10^{-3}$	$4.1 \times 10^{-3}$	$7.5 \times 10^{-4}$	$4.0 \times 10^{-4}$	$9.9 \times 10^{-3}$	$3.4 \times 10^{-3}$	$2.1 \times 10^{-3}$	7.6
M	$2.0 \times 10^{-2}$	$1.0 \times 10^{-2}$	$2.5 \times 10^{-3}$	$1.6 \times 10^{-3}$	$1.2 \times 10^{-2}$	$5.2 \times 10^{-3}$	$3.1 \times 10^{-3}$	11.2
L	$3.9 \times 10^{-2}$	$2.1 \times 10^{-2}$	$5.6 \times 10^{-3}$	$3.2 \times 10^{-3}$	$1.3 \times 10^{-2}$	$6.5 \times 10^{-3}$	$3.7 \times 10^{-3}$	23.2
XL	$4.3 \times 10^{-2}$	$1.5 \times 10^{-2}$	$1.1 \times 10^{-2}$	$5.0 \times 10^{-3}$	$4.6 \times 10^{-3}$	$6.6 \times 10^{-3}$	$4.3 \times 10^{-3}$	43.2
XXL	$4.0 \times 10^{-2}$	$5.0 \times 10^{-3}$	$7.9 \times 10^{-3}$	$7.9 \times 10^{-3}$	$7.8 \times 10^{-4}$	$2.4 \times 10^{-3}$	$3.5 \times 10^{-3}$	47.3
x-S	$1.6 \times 10^{-2}$	$3.9 \times 10^{-3}$	$1.7 \times 10^{-3}$	$1.2 \times 10^{-3}$	$8.0 \times 10^{-3}$	$3.2 \times 10^{-3}$	$2.0 \times 10^{-3}$	4.4
x-L	$3.3 \times 10^{-2}$	$2.3 \times 10^{-2}$	$7.3 \times 10^{-3}$	$2.7 \times 10^{-3}$	$1.4 \times 10^{-2}$	$8.8 \times 10^{-3}$	$4.7 \times 10^{-3}$	37.6
x-XL	$2.7 \times 10^{-2}$	$1.2 \times 10^{-2}$	$1.0 \times 10^{-2}$	$6.4 \times 10^{-3}$	$3.5 \times 10^{-3}$	$6.2 \times 10^{-3}$	$5.6 \times 10^{-3}$	20.2
y-S	$1.2 \times 10^{-2}$	$9.9 \times 10^{-3}$	$2.4 \times 10^{-3}$	$1.1 \times 10^{-3}$	$1.2 \times 10^{-2}$	$5.9 \times 10^{-3}$	$4.1 \times 10^{-3}$	14.4
y-L	$3.0 \times 10^{-2}$	$6.9 \times 10^{-3}$	$3.8 \times 10^{-3}$	$3.1 \times 10^{-3}$	$7.8 \times 10^{-3}$	$3.7 \times 10^{-3}$	$2.3 \times 10^{-3}$	10.8
y-XL	$3.6 \times 10^{-2}$	$5.6 \times 10^{-3}$	$4.1 \times 10^{-3}$	$3.3 \times 10^{-3}$	$5.7 \times 10^{-3}$	$2.6 \times 10^{-3}$	$1.6 \times 10^{-3}$	10.3
LspecMR	$3.7 \times 10^{-2}$	$1.8 \times 10^{-2}$	$5.5 \times 10^{-3}$	$3.1 \times 10^{-3}$	$1.1 \times 10^{-2}$	$6.1 \times 10^{-3}$	$3.6 \times 10^{-3}$	21.8
LspecHR	$4.2 \times 10^{-2}$	$9.8 \times 10^{-3}$	$3.2 \times 10^{-3}$	$2.0 \times 10^{-3}$	$5.8 \times 10^{-3}$	$3.6 \times 10^{-3}$	$2.0 \times 10^{-3}$	23.4
LspecMRs	$4.3 \times 10^{-2}$	$2.4 \times 10^{-2}$	$5.4 \times 10^{-3}$	$3.2 \times 10^{-3}$	$1.4 \times 10^{-2}$	$6.1 \times 10^{-3}$	$3.9 \times 10^{-3}$	10.9
MspecMRb	$1.9 \times 10^{-2}$	$8.6 \times 10^{-3}$	$2.6 \times 10^{-3}$	$1.6 \times 10^{-3}$	$1.0 \times 10^{-2}$	$5.3 \times 10^{-3}$	$3.1 \times 10^{-3}$	26.4
L-SAFI	$3.9 \times 10^{-2}$	$2.1 \times 10^{-2}$	$5.3 \times 10^{-3}$	$3.2 \times 10^{-3}$	$1.2 \times 10^{-2}$	$6.1 \times 10^{-3}$	$3.9 \times 10^{-3}$	25.6
XL-SAFI	$4.8 \times 10^{-2}$	$2.4 \times 10^{-2}$	$1.0 \times 10^{-2}$	$5.4 \times 10^{-3}$	$7.0 \times 10^{-3}$	$6.2 \times 10^{-3}$	$4.8 \times 10^{-3}$	48.6

Notes. Column 1: name of run. Column 2: root-mean-square density  $\rho_{\text{rms}} = \sqrt{\langle(\rho - \bar{\rho})^2\rangle}$ . Columns 3-5: Fourier amplitude of radial density modes  $k_x = 1 \dots 3$ , normalized by mean density in the box. Columns 6-8: Fourier amplitude of azimuthal velocity modes  $k_x = 1 \dots 3$  with  $\hat{u}_y = u_y - \bar{u}_y$ . Column 9: correlation time, in orbits  $T = 2\pi\Omega^{-1}$ , of the largest radial density mode.

i.e., regions where the azimuthal gas velocity is higher than the pressure-supported Keplerian flow.

#### 4.1. Particles in Zonal Flows

In the upper right panel of Figure 5, the azimuthal gas velocity development of run *XXL* is shown, overplotted with the position of the most massive clump for each time step. The azimuthal gas velocity coincides with the derivative of the gas density, but it is much easier to interpret. The speckled structure of the derivatives comes due to the high power in the smaller scales. However, the large-scale structure is still visible and the geostrophic correlation between the structures of  $u_y(x, t)$  and  $d/dx[\rho(x, t)]$  is directly observed. Since they have the same large-scale structure, the particle position is much easier interpreted at the azimuthal gas velocity plot than on the density gradient plot. Sometimes the radial displacement from one orbit to the next is too large to be explained by radial drift. That happens when another clump becomes more massive than the previous one. These particles accumulate in regions with high azimuthal gas velocities (see upper right panel in Figure 5). The only time when this is not true is at times from 80 to 100 local orbits. In this period, an inward-drifting clump stayed coherent during the time of its drift. The drift velocity of the most massive particle clump is indirectly encrypted in this plot. Particles are drifting much slower when they are trapped by a pressure gradient. As all particles drift inward this leads to accumulation of particles in regions where the perturbed pressure gradient is positive.

The maximal accumulation of particles for runs *XL* and *y-S* are plotted in the top panel in Figure 7. The second panel shows the evolution of the quantity  $\sqrt{\langle u_y - \langle u_y \rangle_{yz} \rangle_x^2}$ , a measure for the strength of the zonal flows. The third panel in Figure 7 shows the evolution of the strength of the gas density enhancement as  $\sqrt{\langle \rho - \langle \rho \rangle_{yz} \rangle_x^2}$ . Comparing the second and third panels,

one can see a clear correlation between the zonal flow strength and the gas density enhancements. The bottom panel in Figure 7 shows the evolution of the  $\alpha$ -parameter, calculated as in Equation (14).

The maximum of the dust overdensity that occurs during one simulation is plotted against the box size in the upper panel of Figure 8. The general trend shows that radially larger boxes have higher particle concentrations. An increased azimuthal extent does not have an effect on the particle concentrations. The most surprising result is in run *y-S*. It shows a very high particle concentration that occurs early in the simulation (compare Figure 7). This is most likely a stochastic coincidence. The lower panel in Figure 8 shows a plot of the maximum dust overdensity against the correlation time of the zonal flows. The error margin are calculated with the standard deviation of the temporal evolution of the two quantities. We see a clear trend that denser particle accumulations develop with longer correlation times. The distribution can be fitted by a power law. This gives an exponent of  $d \log \rho / d \log \tau_{\text{corr}} = 0.38 \pm 0.05$ . The one point that does not overlap with the error margins of the fit is from run *y-S*. If we take the maximum of the top panel in Figure 7 after the two first maxima (i.e., after  $45T_{\text{orb}}$ ) and plot this value again in the parameter space of Figure 8, we get the position marked with the blue square. It agrees well with the error margins of the fit.

In isothermal geostrophic balance,  $2\rho\Omega u_y = c_s^2 \partial \rho / \partial x$ , the azimuthal gas velocity follows the radial density gradient. That this is true for large scales as shown in Figure 9. The upper left panel shows the evolution of the azimuthally and vertically averaged azimuthal component of the gas velocity. Overplotted are the locations of the maxima in the dust density. In the upper right panel the dust density evolution of the same run *L* is plotted. In comparing the location and times of the maxima and minima on these two plots, one clearly sees that maxima in the dust density occur often at times and loca-



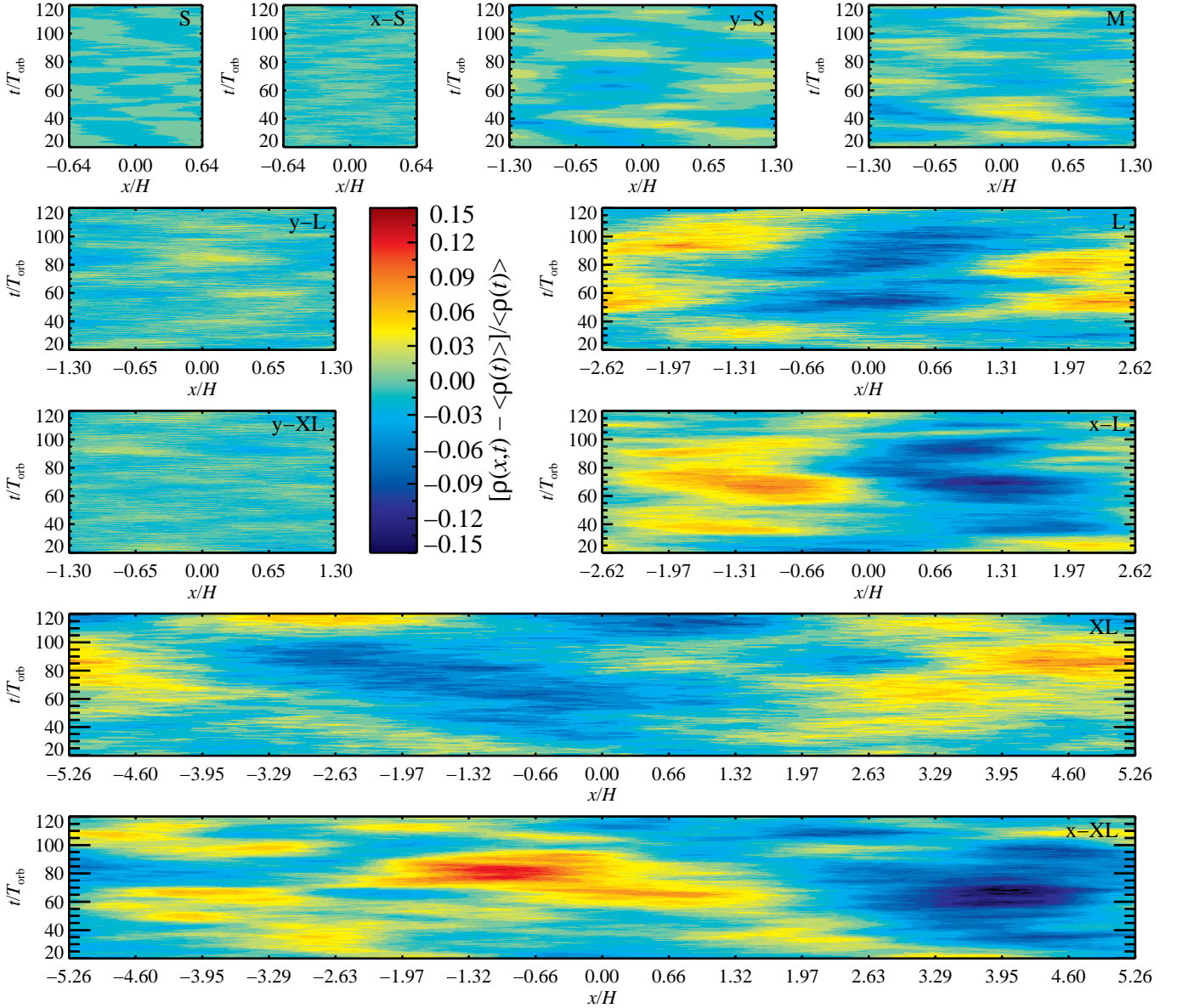


**Figure 4.** Evolution of the gas density perturbation of all runs from simulation sets *A*, *B*, and *C*. Run *XXL* is shown in Figure 5. The density is averaged in vertical and azimuthal direction and plotted in radial direction over time. The lifetime, the size, as well as the strength of the pressure bumps are clearly increasing with increasing box size in simulation set *A*, i.e., runs *S*, *M*, *L*, *XL*, and *XXL*. In simulation set *B*, i.e., runs *x-S*, *M*, *x-L*, and *x-XL*, we have the same increase of lifetime, size, and strength of the pressure bumps. Only for the very large simulation ( $L_x = 10.56H$ ), there is no apparent difference in pressure bump size and strength to run *x-L*. For simulation set *C*, i.e., runs *y-S*, *M*, *y-L*, and *y-XL*, the strength of the pressure bumps is apparently constant throughout this set of simulations. Even the lifetime decreases slightly with increasing box size.

tions where one finds maxima in the gas velocity. Two attempts to quantify this observation are shown in the lower row of Figure 9. In the left panel, the particle density and the azimuthal velocity from the two upper panels are plotted against each other, regardless of position and time. In the right panel, a snapshot of the simulation (as in Figure 2) was taken at 85 local orbits, the time when the maximum dust density enhancement occurs. The particle density as well as the azimuthal gas velocity were integrated in vertical direction and plotted against each other, regardless of their radial or azimuthal position in the simulation, in this scatter plot. In order to visualize high densities of points in these plots, we computed a two-dimensional histogram of the scattered

points. This is indicated by the color scale, showing the amount of points in each of the boxes in the scatter plot space. There is a clear trend for high dust density concentrations to appear at high gas velocities. Without radial drift particles would concentrate where  $u_y = 0$ , i.e., between the sub- and super-Keplerian flow. Due to the radial drift particles accumulate slightly downstream at the formed pressure bumps. Those happen to be at the maxima of the azimuthal gas velocity. With the geostrophic balance, high velocities are also regions of a high radial density gradient. These plots prove that the particles in the simulations are trapped by the long-lived pressure gradients that occur due to stable zonal flows.

If the dust-to-gas ratio increases to values larger than

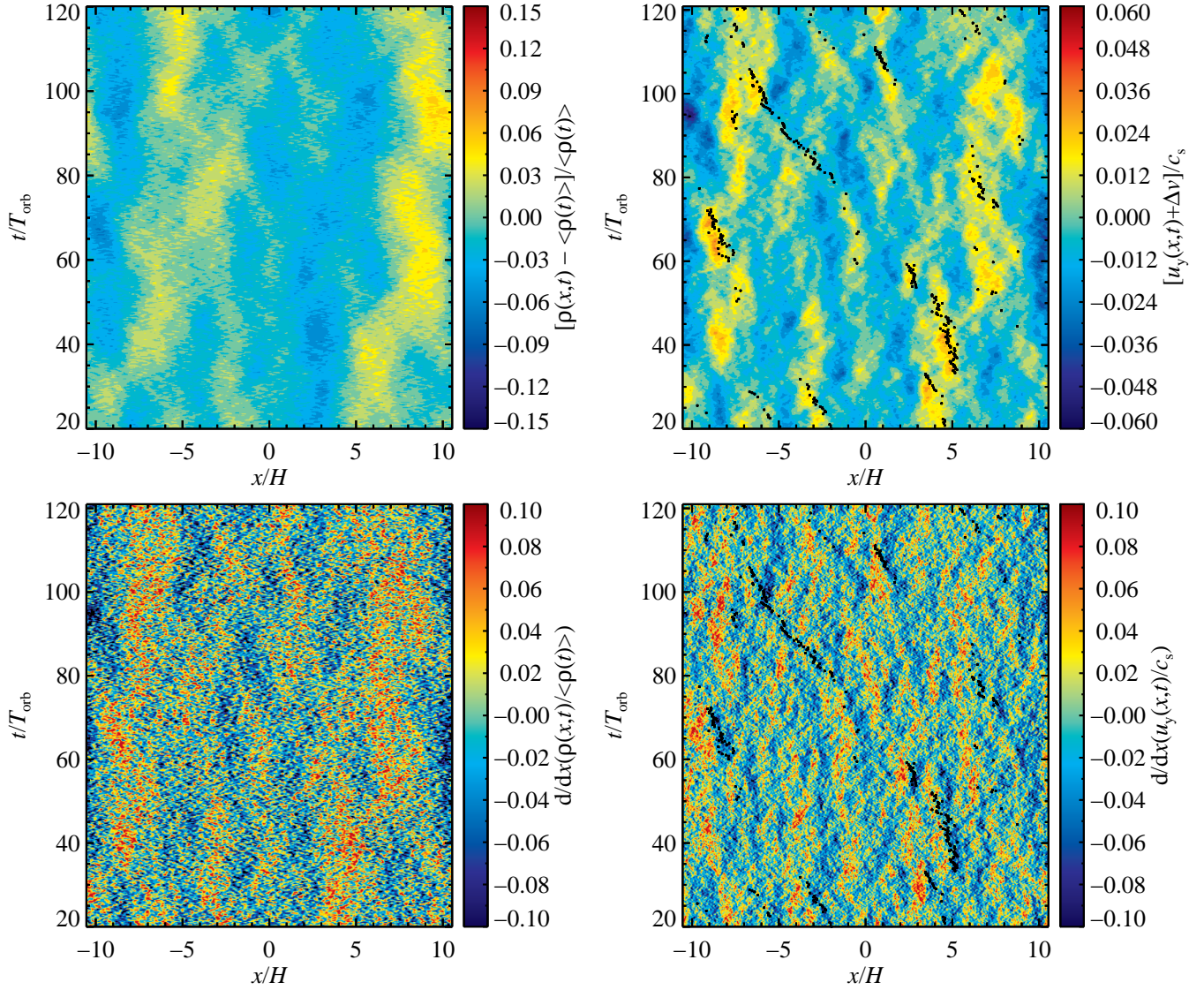


**Figure 5.** Top panels show the evolution of the gas density perturbation and the azimuthal gas velocity of run *XXL*, whereas the bottom row shows the radial derivative of these quantities. The derivatives are very speckled, since small-scale fluctuations give stronger amplitudes to the derivatives. However, the underlying large-scale structure is still visible. The azimuthal gas velocity follows the radial gas density gradient, as expected for a geostrophic balance. Hence, it is possible to interpret the radial derivative of the azimuthal gas velocity as the second derivative of the gas density. In the upper right panel, the black dots represent the position of the most massive particle clump in the simulation at each time. It is clearly shown that particles get trapped in regions of positive zonal flow downstream of pressure bumps.

unity, the streaming instability (Youdin & Goodman 2005; Johansen & Youdin 2007; Youdin & Johansen 2007) is triggered. This increases the dust density further on timescales shorter than an orbital period. To follow the streaming instability development, the back-reaction of the dust particles to the gas phase must be considered in future numerical simulation. This effect was neglected in this set of simulations. Otherwise the initial dust-to-gas ratio would have been an additional free parameter to be studied.

#### 4.2. Radial Drift

Radial drift velocities of the particles in the simulations with different box sizes are shown in Figure 10. The upper panel shows the measured and expected radial drift of two simulations (*M* and *XL*). They show that particles drift slower in turbulent simulations than

they would in a laminar disk. However, the size of the simulation has little effect on the actual drift velocity, as shown in the lower panel of Figure 10. It shows a time average of the particle drift velocity plotted against the box size. The uncertainties are too large to reveal a trend. Thus, the reduction of the radial drift velocity apparently only depends on the amplitude of the zonal flow, but not on the correlation time. Looking at the largest run *XXL*, we can estimate that the radial drift gets reduced by about 28% (drop of the absolute value from  $0.05c_s$  to  $(0.036 \pm 0.003)c_s$ ).

#### 4.3. Clustering

The clustering degree of the particle distribution can be estimated with the distribution of the dust surface density  $\Sigma_p$  (Pan et al. 2011). The initial distribution is

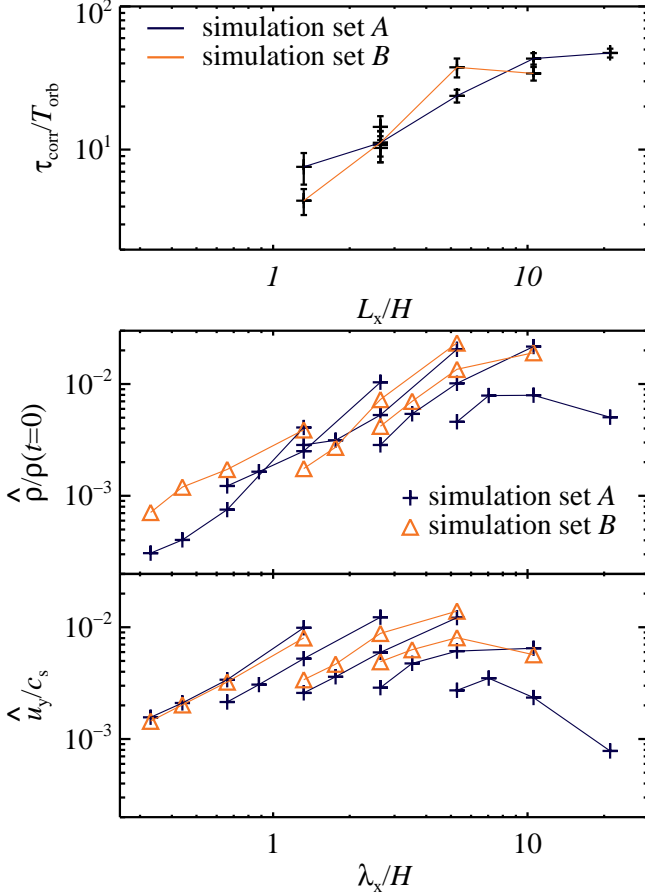


**Figure 6.** Upper plot shows the correlation times of the largest radial density mode against the radial box size. The lines correspond to the simulation sets A and B. The results from simulation set C are omitted for visibility. The correlation time  $\tau_{\text{corr}}$  grows for boxes with a larger radial extent. Only run *x-XL* does not follow this trend. The large ratio  $L_x/L_y$  may prohibit formation of stable zonal flows. The two lower plots show the first four amplitudes of the radial Fourier modes of the gas density and the azimuthal gas velocity against their real size  $\lambda_x = L_x/k_x$ ;  $k_x$  is the wave number of the corresponding Fourier mode, defined by  $\omega_x = 2\pi k_x/L_x$  in the Fourier mode  $\sin(\omega_x x)$ . The lines connect the amplitudes of different Fourier modes for one simulation. Both quantities have most of their power in the largest modes. Only in the largest simulations, the power in the largest modes decreases. There the maximum is between  $5H$  and  $7H$ .

represented by a Poisson distribution (see Figure 11).<sup>6</sup> For this plot, we binned the measured dust surface density of a snapshot. We then normalized them to the amount of grid cells. About three local orbits after the particles feel the gas drag, the shape of the distribution function is saturated. We averaged the distribution over the time of  $23 \dots 121T_{\text{orb}}$ . We see at the high density end of the distribution that higher densities develop in larger boxes due to the higher number of available particles. Thus, the clustering properties do not depend strongly on the strength or lifetime of the zonal flows (compare Figure 8, bottom).

#### 4.4. Different Particle Sizes

So far we only considered simulations with one particle species, i.e.,  $\text{St} = \tau_f \Omega = 1$ . We take the simulation

<sup>6</sup> Run *XXL* was not included in this figure, because the number of particles per grid cell was different to the other runs.

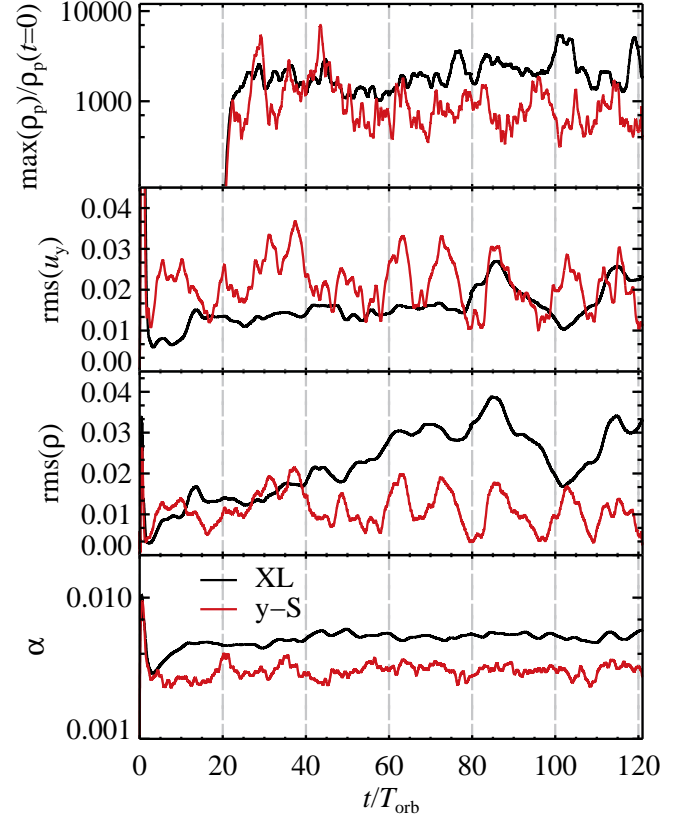


**Figure 7.** Time series of runs *XL* and *y-S*. The plots show (from top to bottom) the maximum of the dust density, the root mean square of the azimuthal gas velocity and the gas density, and the  $\alpha$ -value (Equation (14)). The dust overdensities of run *XL* have a higher base than those of run *y-S*. The latter has some spikes in the beginning, but is lower for most time of the simulation. The two panels in the middle show that the azimuthal gas velocity and the gas density are correlated. Both plots show maxima and minima at the same time, while  $\alpha$  is rather stable with time. The time-averaged  $\alpha$ -values for all simulations can be found in Table 2.

size that simulates one fully extended zonal flow and investigate 12 different particle species. The particle sizes range from  $\text{St} = 0.01$  to  $\text{St} = 100$ . We choose run *L* with the dimensions  $5.28H \times 5.28H \times 2.64H$  as simulation size for the last simulation set. For one simulation we used a smaller box, because the integration time had to be increased by a factor of two to give the particles with the high Stokes numbers the opportunity to react on the pressure differences.

##### 4.4.1. Drift Velocity and Particle Densities

The results are shown in Figure 12. The upper left panel shows the negative of the radial velocity of the particles, averaged over all particles of a certain size and over time. The four different simulations match very well. The plot shows that particles with  $\text{St} = 1$  drift fastest inward, also with turbulence in the simulations. On both sides the inward drift velocity decreases with similar slopes. The key to the different colors and symbols is in the lower right panel. Overplotted, in a dashed gray line, we find the analytical prediction (following Equation (12)) for the radial drift in a laminar disk. The difference to the prediction is shown in the lower sub-panel. Large particles generally drift slower according to the steady-state solution and their coupling to the gas is also much



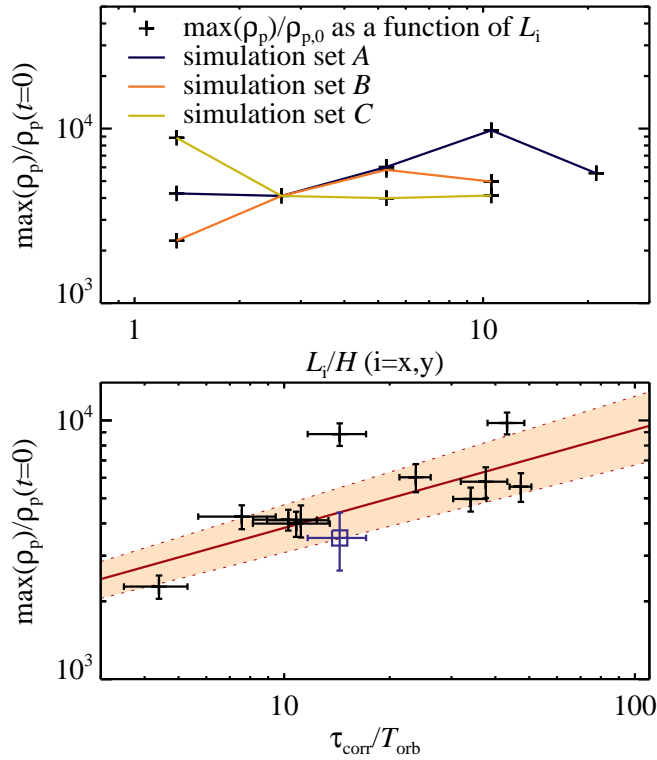


**Figure 8.** In the upper panel, the highest peak in the time series of the dust overdensity (the top panel in Figure 7) is plotted against the size of the simulation box. The diagonal simulation set A is marked by the blue line. The dust overdensity increases with box size, until it suddenly drops for the largest box. In simulation set B (red), the quantity saturates for boxes with a radial extent that is twice as large as the azimuthal extent or larger. When keeping the radial extent constant (simulation set C, yellow line), the maximum saturates for the cubic box case. Hence, the only in azimuthal direction extended boxes do not lead to an artificial enhancement of the dust overdensities. The very high overdensity for run *y-S* seems to be a stochastic coincidence (compare top panel in Figure 7). The lower panel shows the dust overdensity against the correlation time. The measured points can be approximated with a power law (shown as a red solid line) with an exponent of  $0.38 \pm 0.05$ . The shaded region, with the dashed red lines as edges, gives the uncertainty of the fit. The one cross off the fit shows the results for run *y-S*. The blue square marks its position, if we neglect the two maxima shown in Figure 7. It overlaps well with the fit region.

weaker. Hence their radial drift velocity is almost not affected by the turbulence and they do not show strong concentrations. Small particles with low Stokes numbers are stronger coupled to the gas and, thus, also drift very slow. Particles with  $St \sim 1$  are concentrated most by the zonal flow and, thus, have a stronger decreased radial velocity. Thus, the accumulation of dust particles is expected to be strongest for particles with Stokes numbers around unity. For  $St = 0.01$  particles, the drift velocity is strongly determined by the gas flow. This explains the strong deviation from the expected drift velocity.

The upper right panel shows the total particles overdensity normalized to the initial particle number density. For run *LspecMR* (black diamonds), the smallest particles have higher concentrations than in the other simulations. This resulted from the choice of too few particles per grid cell. There only 100,000 particles per size bin were simulated. This results in overestimation, because the number density is normalized with the initial number density  $n_0$ . For example, run *LspecMRs* (red

squares) follows 2,000,000 particles per particle size bin. The highest concentrations were reached for particles of sizes  $St = 0.75 \dots 5$ , as expected. However, the exact peak has a stochastic factor to it. Thus, the simulations peak at different particle sizes. The overdensities are more investigated in the lower row of panels.

The surface number density of the particles is shown in the lower left panel. Here, the particles were integrated in the vertical direction. The trend is similar to the upper right panel. We read from this plot that particles with  $St = 0.1$  are concentrated about ten times the initial concentration. Together with the vertical overdensity due to sedimentation (lower right panel), a total overdensity of about 100 is created for  $St = 0.1$  particles.

The peaks in the vertical density structure of the particles are shown in the lower right panel of Figure 12. The Stokes number,  $St = \tau_f \Omega$  defines the timescale after which the particles are settled down to the mid-plane. Particles with a high Stokes number are not fully settled down to the mid-plane, not even in the long-integration run *MspecMRb*. The resolution also limits this measurement for particles that are very close to the mid-plane. Smaller particles are not that strongly stratified. Thus, the vertical (Gaussian) structure is wider and shallower. This results in a lower value in this plot. The points for Stokes numbers 0.01–1 follow a power law with the index of  $0.58 \pm 0.03$ . The measured power law index is slightly higher than the expected value of 0.5 (Dubrulle et al. 1995). Most of the particles with  $St \gtrsim 1$  sediment very close to the mid-plane. This prohibits a further increase in the vertical density. A higher resolution and a measurement of the dust scale height is achieved in the next section.

#### 4.4.2. Dust Pressure Scale Height

With a stratified particle distribution we can test the vertical diffusion model (see, e.g., Carballido et al. 2006). The dust pressure scale height can be directly calculated from the vertical positions of the particles of the same size. It is approximately proportional to  $St^{-0.5}$  in agreement with Carballido et al. (2006, 2011) and Youdin & Lithwick (2007). The results are summarized in the upper panel of Figure 13. Since the analytical value was calculated with the  $\alpha$ -value, the vertical Schmidt number

$$Sc_z = \frac{H_{p, \text{expected}}}{H_{p, \text{measured}}} \sim \left( \frac{\alpha}{D_T(\infty)} \right)^{\frac{1}{2}} \quad (16)$$

can be calculated. We measured the vertical Schmidt number to have a very weak dependence on the particle size. In the lower panel of Figure 13 we show that  $Sc_z = 3.4 \cdot St^{0.11}$ .

## 5. DISCUSSION AND CONCLUSIONS

### 5.1. Zonal Flows and Axisymmetric Pressure Bumps

Our simulations have dimensionless units. This allows us to interpret our results manifold. We can pick the distance to the star in a certain range. In Section 2.5, we defined the global pressure gradient to be  $\Delta v = 0.05 c_s$ . In the minimum mass solar nebula (MMSN) model, we can choose the distance to the star to be between 0.35 and 40 AU (Hayashi 1981). For this discussion, we pick



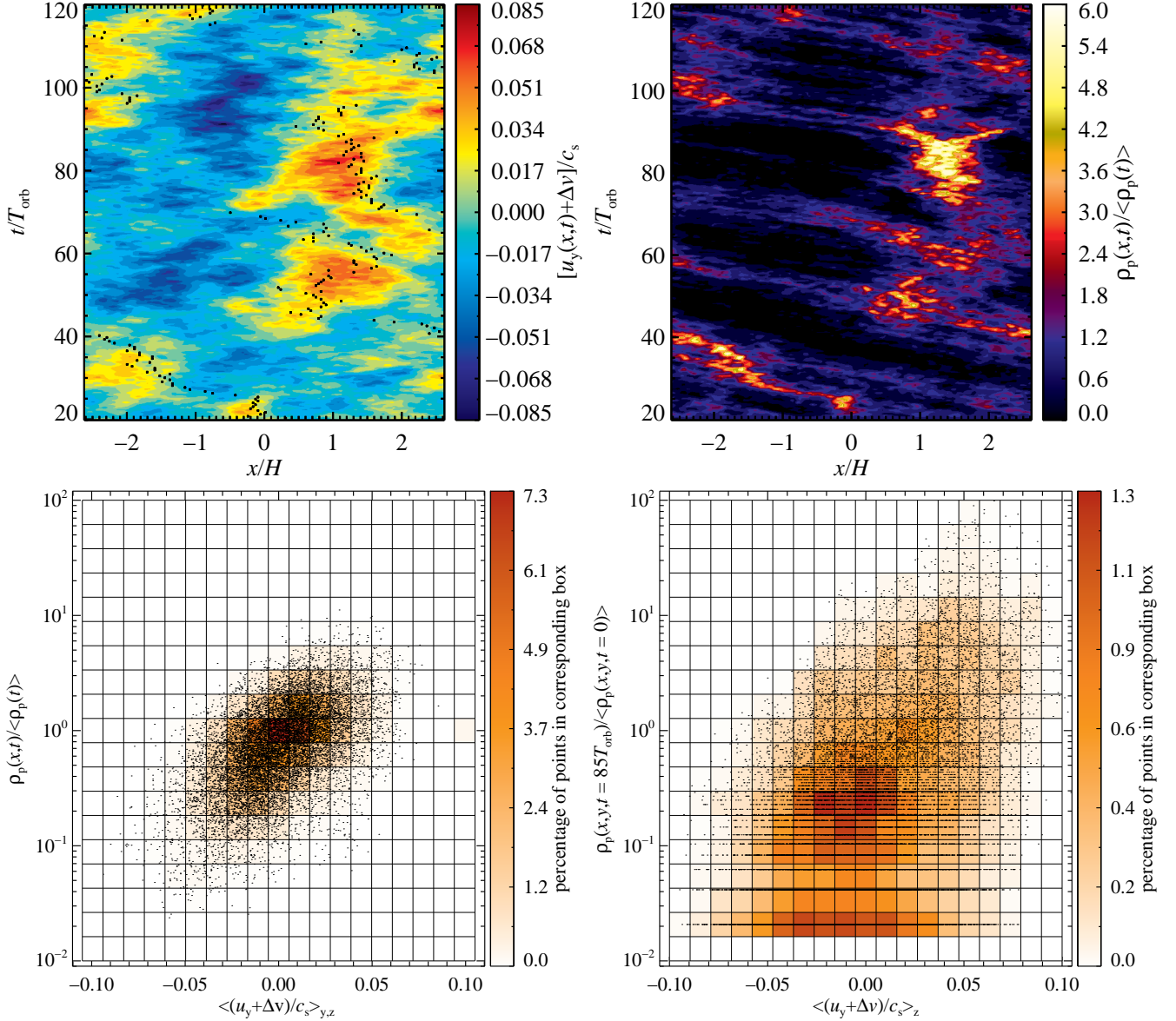


**Figure 9.** Top row shows the evolution of the azimuthal gas velocity and the dust density evolution of run *L*, respectively. The quantities are averaged in vertical and azimuthal direction and plotted in radial direction over time. The black dots in the upper left panel show the position of the highest dust density at each orbit. This shows that the overdensities of the dust often appear at places and times where the azimuthal gas velocity is high. This relation shows that the zonal flows accumulate dust and are a possible venue of planetesimal formation. The bottom left panel shows a scatter plot of the dust density  $\rho_p$  against the azimuthal gas velocity, where both values are averaged in vertical and azimuthal direction, as in the upper panels. The bottom right panel shows a plot of the particle surface density  $\rho_p(x,y,t)$  in relation to the azimuthal gas velocity, averaged in vertical direction, computed from a snapshot taken at  $85T_{\text{orb}}$ , the time when the maximum in the dust density occurs. Both plots show that it is more likely to find a high dust density at a location where the azimuthal gas velocity is high.

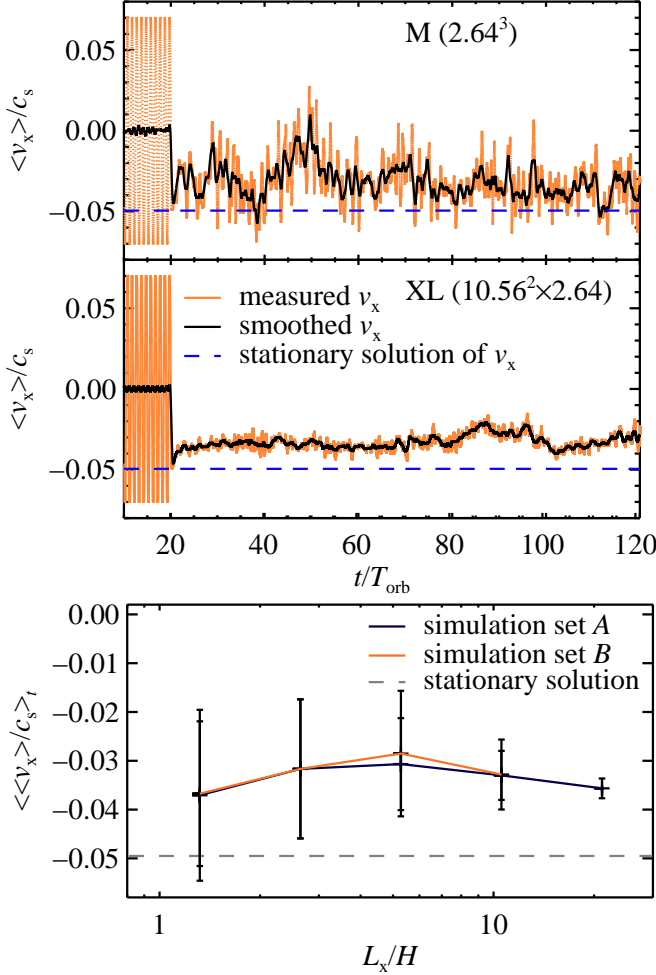
$r = 5 \text{ AU}$ . In a thin disk model, we get a ratio for  $H/r \sim 0.033(5 \text{ AU/AU})^{1/4} \sim 0.05$ ; this defines us  $H = 0.25 \text{ AU}$ . The isothermal sound speed is  $c_s = H\Omega \sim 66,000 \text{ cm s}^{-1}$ . Thus, turbulent velocities ( $u_{\text{rms}}$ ) are about  $9000 \text{ cm s}^{-1}$  ( $\sim 7000 \text{ cm s}^{-1}$  for the high-resolution run *LspecHR*).

Figure 14 shows the highest azimuthal velocity for all simulation sizes. We averaged over several maxima of  $u_y(x,t)$  for every simulation to smooth over outliers. The zonal flows are super-Keplerian for all but runs *XXL*, *x-S*, and *y-XL*. In the largest box the flow only reaches slightly sub-Keplerian velocities. However, particles still get captured in the resulting axisymmetric pressure bumps. The speeds measured in the largest simulation match those

measured in Flock et al. (2011).

We measured the radial size of the axisymmetric pressure bumps to be between 5 and  $7H$  (see Figure 6). At a distance of 5 AU to the star, this size corresponds to  $\sim 1.25 \dots 1.75 \text{ AU}$  radial size for zonal flows, i.e., the distance between peaks of  $\langle \rho \rangle_{yz}$ . This measurement agrees well with Simon et al. (2012) who measured the radial size of their zonal flows to be  $6H$ . Further studies with varying box size in smaller steps could potentially narrow down the radial scale.

We measured the lifetimes of the zonal flows up to  $50T_{\text{orb}}$ . This agrees well with earlier stated lifetimes (Johansen et al. 2009a; Uribe et al. 2011). The strength



**Figure 10.** Radial drift velocity of the particles for two different simulations is shown in the upper panel. Particles in these simulations all have a Stokes number of  $St = \tau_f \Omega = 1$ . The orange lines are the exact measured radial velocities, averaged over all particles. The black line represents the same value smoothed over the time of one local orbit. The blue dashed line shows the analytical result in a stationary box for particles of  $St = 1$  following Equation (12). Particles in turbulent simulations generally drift slower than expected from the stationary solution, but the box size has little effect on the drift velocity. This is shown in the lower panel where the mean of the radial drift velocity is plotted against the box size. We omitted simulation set *C* for visibility. There is a minimum in drift speed for run *L*. However, this minimum is within the error margins. The smallest errors are with run *XXL*; here the drift velocity drops by 28%.

of the density bump reaches 15% and goes down to about 10% in the largest simulation. The lower amplitude is consistent with the results from global simulations (private communication with Mario Flock about the simulations from Flock et al. 2011, 2012) who measured a density enhancement of slightly less than 10%. Some works (e.g., Uribe et al. 2011; Simon et al. 2012) measure stronger density enhancements. A possible explanation is that their  $\alpha$  values are higher than in this work. Further studies on the dependence of volume average quantities to strength of zonal flows would be interesting.

### 5.2. Dust in Zonal Flows

Particles get trapped downstream of pressure bumps and build up overdensities. To compare our dimensionless particle sizes with collision experiments and observa-

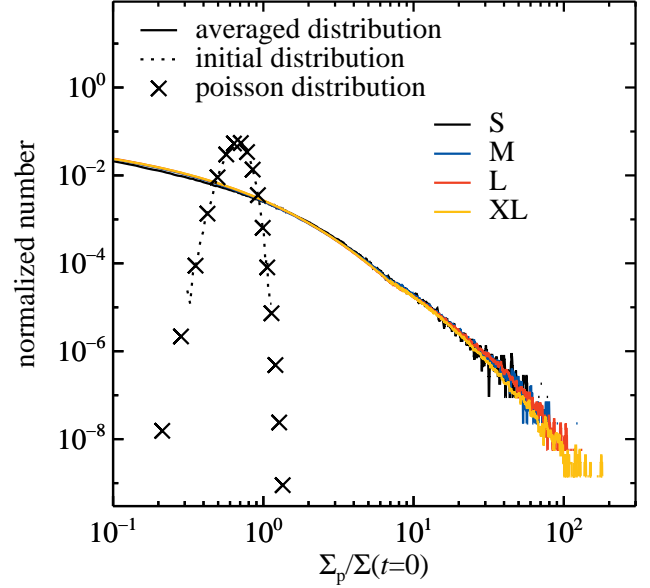


**Figure 11.** Distribution of the dust-to-gas ratio of the surface densities for runs *S*, *M*, *L*, and *XL*. For comparison a Poisson distribution is shown with crosses. The initial distribution of the numerical simulation (dotted line) fits very well to the normal distribution. The average strength of the clustering for the dust surface density does not depend on the simulation box size.

tions we have to assume a distance to the star and pick a solar system model. This will allow us to discuss our results in context to recent experiments.

By choosing a model for the solar system, we can convert the dimensionless Stokes number  $St = \tau_f \Omega$  to a real particle size. The friction time  $\tau_f$  correlates to the particle radius  $a$  with

$$a = \frac{\tau_f^{(Ep)} \Omega \Sigma_{\text{gas}}}{\sqrt{2\pi} \rho_{\bullet}}, \quad (17)$$

for Epstein drag and

$$a = \sqrt{\frac{9\tau_f^{(St)} \Omega \mu H}{4\rho_{\bullet} \sigma_{\text{mol}}}}, \quad (18)$$

for Stokes drag (see supplementary info for Johansen et al. 2007). Here  $\Sigma_{\text{gas}}$  is the column density of the gas,  $\rho_{\bullet}$  is the density of solid material,  $\mu = 3.9 \times 10^{-24} \text{ g}$  is the mean molecular weight, and  $\sigma_{\text{mol}} = 2 \times 10^{-15} \text{ cm}^2$  is the molecular cross section of molecular hydrogen (Nakagawa et al. 1986; Chapman & Cowling 1970).

The Epstein regime applies, if the particle radius  $a$  does not exceed  $(9/4)$  (Weidenschilling 1977a) of the gas mean-free path

$$\lambda = \frac{\mu}{\rho_{\text{gas}} \sigma_{\text{mol}}} = \frac{\sqrt{2\pi} \mu H}{\Sigma_{\text{gas}} \sigma_{\text{mol}}}. \quad (19)$$

The gas density and hence also the particle size for a given Stokes number  $St = \tau_f \Omega$  depends very much on the used model. In Figure 15 we overview four different models. The MMSN (Weidenschilling 1977b; Hayashi 1981) was calculated from the mass of the existing planets, neglecting migration. Because this model allows no mass loss through accretion, often 3-MMSN is used to account

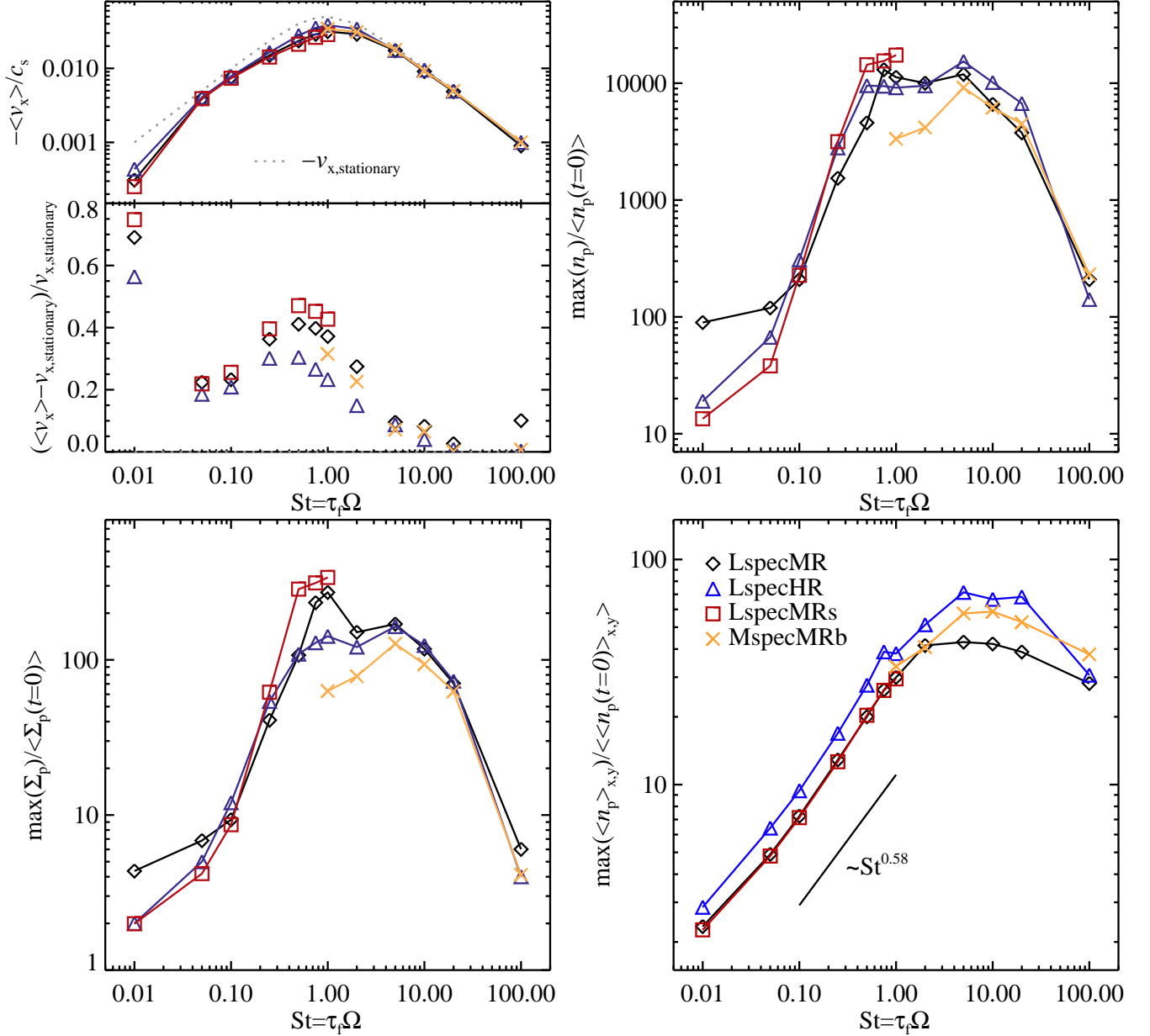


**Figure 12.** These panels show the behavior of particles with Stokes numbers from 0.01 to 100. The upper left panel shows the negative of the radial drift velocity and the relative difference between the measured and expected drift velocity. The dashed gray line shows the stationary solution for the radial drift, following Equation (12). The highest drift velocities are obtained for particles with  $St = 1$ , but they are also slowed down strongest by the MRI-turbulence. The upper right panel shows the highest overdensity that occurred for the specific particle size during the entire simulation. The slopes for the different simulations match very well, apart from a jump around  $St = 1$  (for *LspecMRs* and *MspecMRb*) and an offset for run *LspecMR* at small particle sizes. The former can be explained with the usage of a smaller simulation box for run *MspecMRb* ( $2.64^3$  with weaker zonal flows) than in the other simulations ( $5.28^2 \times 2.64$  with stronger zonal flows). The offset showed that the number of particles per particle size was not sufficient in run *LspecMR* ( $10^5$  particles in  $\sim 1.5 \times 10^6$  grid cells leads with five particles in one grid cell to a result of  $\max(n_p) / \langle n_p(t=0) \rangle = 75$ ). The lower left panel shows the maximum of the column density for each particle size. It peaks at sizes of around  $St = 1$ . The lower right panel shows the maxima of the vertical distribution of particles. The curves (for  $St = 0.01 \dots 1$ ) follow a power-law with the index of  $0.58 \pm 0.03$ . This is slightly steeper than the expected power law index of 0.5 (Dubrulle et al. 1995). In all four plots, the results of particles with  $St = 0.01$  are to be interpreted with caution, because the simulations lacked sufficient amount of super-particles for these size bins. Further, large particles ( $St = 100$ ) did not have enough time to sediment to the mid-plane.

for some accretion. A low-density model was published by Brauer et al. (2008). This model is adopted from measurements that indicate a shallow surface density profile for protoplanetary disks (Andrews et al. 2010). The high-density model was adopted from Desch (2007), who introduced a “revised MMSN model” by using the starting positions in the Nice model of planetary dynamics

(Tsiganis et al. 2005). This model also takes planetary migration into account. The equations used to calculate

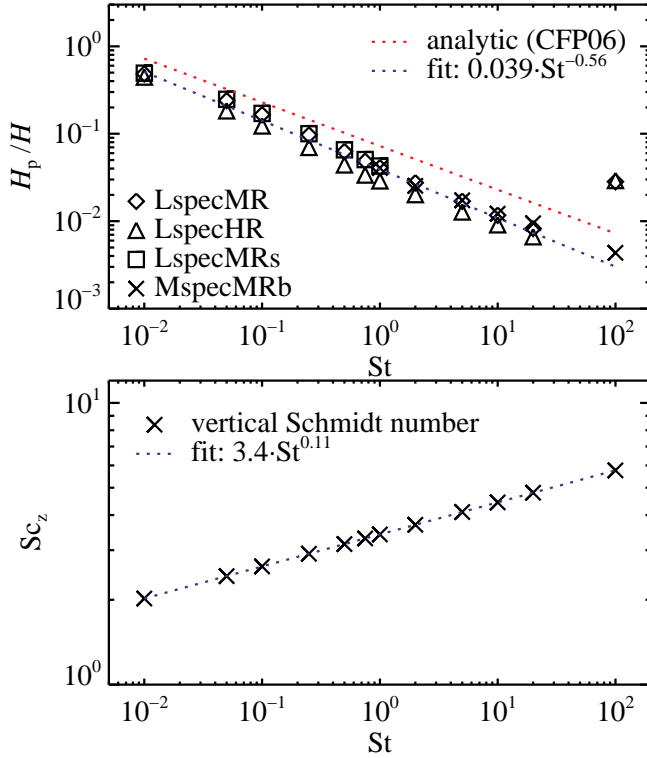


**Figure 13.** Dust scale height as a function of the Stokes number is shown in the upper panel. Different symbols depict the different simulations. The expected dust scale height is calculated after Carballido et al. (2006) and compared with the fitted function. This value is the vertical Schmidt number  $Sc_z$ , shown in the lower panel. Its dependence on the particle size is very weak.

the particle sizes in Figure 15 are

$$\Sigma_{\text{gas}} = \begin{cases} 1700 \frac{\text{g}}{\text{cm}^2} \left(\frac{r}{\text{AU}}\right)^{-1.5} & (\text{MMSN}) \\ 5100 \frac{\text{g}}{\text{cm}^2} \left(\frac{r}{\text{AU}}\right)^{-1.5} & (3 \cdot \text{MMSN}) \\ 683 \frac{\text{g}}{\text{cm}^2} \left(\frac{r}{\text{AU}}\right)^{-0.9} & (\text{low density}) \\ 51,000 \frac{\text{g}}{\text{cm}^2} \left(\frac{r}{\text{AU}}\right)^{-2.2} & (\text{high density}). \end{cases} \quad (20)$$

Throughout the discussion, we assume the MMSN model at 5 AU distance to the star for size reference for our test particles. This choice affects only the translation from the Stokes number  $St$  to a size, not the dynamics in our models.

If the local dust density exceeds the Roche density, a clump is gravitationally bound against shear. The Roche density can be approximated (Kopal 1989) by

$$\rho_{\text{Roche}}(R=5 \text{ AU}) = \frac{9}{4\pi} \frac{\Omega^2}{G(R=5 \text{ AU})} \sim 100\rho(R=5 \text{ AU}), \quad (21)$$

for an MMSN.  $G$  is the gravitational constant. The streaming instability (Youdin & Johansen 2007; Johansen & Youdin 2007) starts to act at dust-to-gas ratios of order unity. We started all our simulations with  $\epsilon_0 = \rho_p(t=0)/\rho = 0.01$ . Thus, a concentration of  $\max(n_p)/\langle n_0 \rangle = 100$  corresponds to  $\epsilon_{\text{streaming}} = 1$ . The Roche density at 5 AU in an MMSN can be expressed as  $\epsilon_{\text{Roche}} = \rho_{\text{Roche}}/\rho \sim 100$ . We can see that objects of several decimeters up to some meters reach  $\epsilon_{\text{Roche}}$ , while pebbles of some centimeters up to a decimeter reach  $\epsilon_{\text{streaming}}$  from combining Figures 12 and 15.

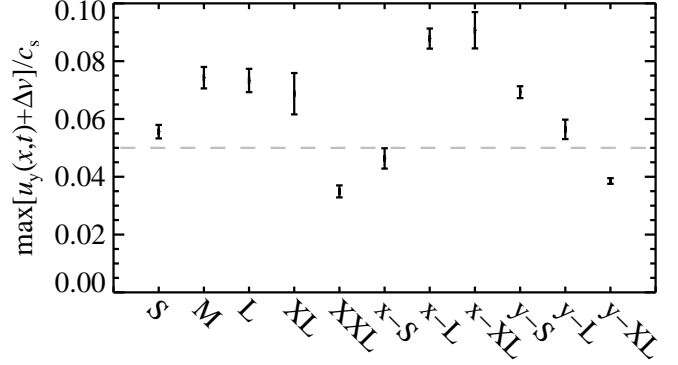


**Figure 14.** Measured highest azimuthal velocity of all box size simulated. The gray dashed line shows the threshold to Keplerian velocity. Only runs *XXL* and *y-XL* do never get super-Keplerian. Simulation *x-S* does get super-Keplerian at some time, but not often enough to be significant.

The concentration factors of run *LspecHR* in the upper right panel of Figure 12 show us that with an initial dust-to-gas ratio of  $\epsilon_0 = 10^{-2}$  particles of sizes  $St = 0.5 \dots 10$  ( $St = 0.1 \dots 0.25$ ) reach a dust-to-gas ratio of 100 ( $\gtrsim 1$ ). These sizes translate to  $30 \dots 400$  cm ( $6 \dots 15$  cm) in an MMSN at a 5 AU orbit using Figure 15. Considering back-reaction from the dust to the gas would allow the streaming instability to act. This will be subject of a future study. In our simulations, we see that the density of  $15 \dots 600$  cm sized icy boulders increases several thousand times over the equilibrium density, even without streaming instability and self-gravity of the particles. Sedimentation to the mid-plane leads to overdensities of around 40, while the contribution from the turbulence concentrates the boulders several hundred times.

Since we do not study the influence of the back-reaction from particles to the gas, we were able to study several particle sizes in one simulation. That also means that the initial dust-to-gas ratio ( $\epsilon_0$ ) can be set arbitrary. We can interpret our results in the light of different metallicities. Particles with  $St \geq 0.5$  will trigger the streaming instability even with  $\epsilon_0 = 10^{-4}$ , while  $St = 0.1$  particles need  $\epsilon_0 = 10^{-2}$ .

At the assumed distance in this discussion, the resulting rings of trapped dust are not observable with current telescopes. If zonal flows form at larger distances to the star and dust rings form at an observable size, they could potentially be observable with ALMA. For an analysis one would have to adjust the parameter  $\Delta v$  to account for the steeper pressure gradient. A preliminary study showed that particles of about 10 cm in size can get capture for a short amount of time at 100 AU distance. However, this question goes beyond the scope of this paper and should be addressed in a future study.

## 6. SUMMARY AND OUTLOOK

We performed numerical simulations of MRI-driven turbulence in shearing boxes, covering the parameter space for radial and azimuthal box sizes up to  $21.12H$ . Further, we followed the reaction of the dust particle density to the turbulence. Our major findings are as follows.

1. Turbulent energy and stresses double when increasing the azimuthal size of the simulation from 1.32 to 2.64 pressure scale heights. Turbulence pa-



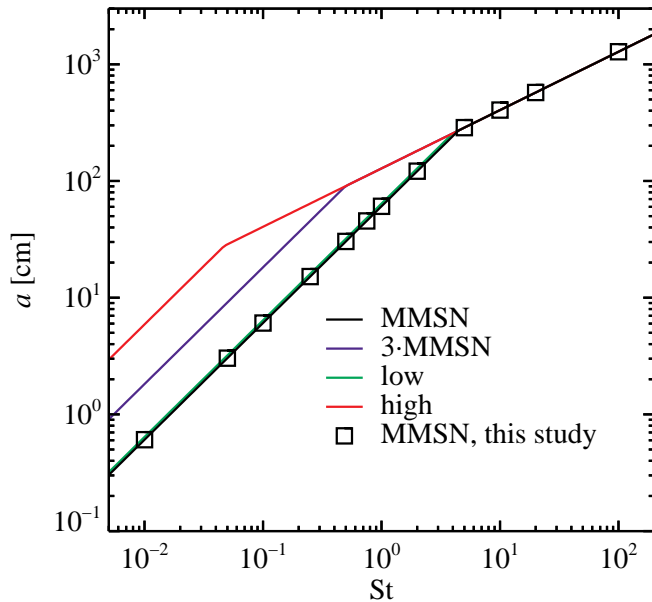


**Figure 15.** Particle sizes as a function of the dimensionless Stokes number for the four discussed models at 5 AU. The black squares show the used Stokes numbers and their corresponding size in the case of the minimum mass solar nebula model.

rameters in radially small box sizes stay approximately constant. This confirms the results in Fromang & Stone (2009). In larger boxes, turbulent fluctuations and stresses are observed to remain constant against changes in the box size (see also Johansen et al. 2009a). This rapid convergence was also observed in Simon et al. (2012).

2. Surface density fluctuations grow to large scales in the box and have lifetimes of up to 50 orbits. The scales of these pressure bumps increase with increasing radial box size, until it saturates at approximately 5–7 pressure scale heights. The scales are decreased when the azimuthal box size is much more increased than the radial box size. The radial scales of the pressure bumps are consistent with the length scales measured in local (e.g., Johansen et al. 2009a; Simon et al. 2012) and global (e.g., Lyra et al. 2008; Uribe et al. 2011) simulations. This might be the natural size of these overdensities. The pressure bumps are in geostrophic balance with sub- and super-Keplerian zonal flows. At 5 AU distance to the star  $6H$  correspond to  $\sim 1.5$  AU. The amplitude of the density bump reaches 15% and goes down to about 10% in the largest simulation.
3. Particles with  $St = \tau_r \Omega = 1$  are getting trapped efficiently by the axisymmetric pressure bumps. They accumulate in regions of minima in the second derivative of the gas density as predicted analytically (e.g., Klahr & Lin 2001). The concentration factor correlates with the correlation time of the zonal flows. Hence, the first two steps of planetesimal formation<sup>7</sup> in protoplanetary disk with an acting MRI are: vertical settling via sedimentation

<sup>7</sup> After coagulation from  $\mu\text{m}$ -sized particles to  $St = 0.1, 1$ .

and radial concentration by trapping of dust in axisymmetric pressure bumps. Further concentration comes likely from stochastic processes. Clustering properties do not depend strongly on strength or lifetime of the zonal flows.

4. We reach dust-to-gas ratios of 50–100. These densities are of the order of the Roche density at 5 AU in an MMSN. The dust overdensities scale with the lifetime of the zonal flow structures by a power law with an exponent of  $0.38 \pm 0.05$  (see Figure 8). To what degree these high dust-to-gas ratios disturb the axisymmetric pressure bumps that developed in the zonal flows has to be investigated in further studies with back-reaction to the gas.
5. Particles of only a few centimeters in size (at 5 AU in an MMSN,  $St = 0.1$ ) accumulate in overdensities that are increased by a factor of  $\sim 100$ , leading to a dust-to-gas ratio of 1 in the mid-plane, thus triggering the streaming instability. Without MRI and zonal flows  $St = 0.1$  particles do not clump strongly and cannot trigger the streaming instability for solar metallicity  $Z = \epsilon_0 = 0.01$  (Johansen et al. 2009b).

This is the first work on the effect from large-scale zonal flows on dust particles in an MHD simulation. Dust gets trapped downstream of long-lived high-pressure regions and achieves overdensities that have the potential to generate streaming instability and to become gravitationally unstable. Planetesimal formation in large boxes will be further investigated in simulations with particle feedback on the gas and self-gravitating particles in a future study.

In the future, we will focus on one model and study various initial dust-to-gas ratios and particle size distributions. We will probably use the already converged run  $L$  ( $5.28H \times 5.28H \times 2.64H$ ). This choice is also a trade-off between simulation box size and computational expense.

K.D. and H.K. have been supported by the Deutsche Forschungsgemeinschaft Schwerpunktprogramm (DFG SPP) 1385 “The first ten million years of the solar system”; K.D. received further support by the IMPRS for Astronomy & Cosmic Physics at the University of Heidelberg. A.J. was partially funded by the European Research Council under ERC Starting Grant agreement 278675PEBBLE2PLANET and by the Swedish Research Council (grant 20103710). Computer simulations have been performed at the THEO cluster at Rechenzentrum Garching and at the JUGENE cluster in Forschungszentrum Jülich (project number HHD19). We thank an anonymous referee for a very thorough referee report that improved the quality of the paper greatly.

## REFERENCES

- Andrews, S. M., Wilner, D. J., Hughes, A. M., Qi, C., & Dullemond, C. P. 2010, *ApJ*, 723, 1241  
 Balbus, S. A., & Hawley, J. F. 1991, *ApJ*, 376, 214  
 Balbus, S. A., & Hawley, J. F. 1998, *RvMP*, 70, 1  
 Beitz, E., Güttler, C., Blum, J., et al. 2011, *ApJ*, 736, 34  
 Birnstiel, T., Klahr, H., & Ercolano, B. 2012, *A&A*, 539, A148  
 Blum, J., & Wurm, G. 2008, *ARA&A*, 46, 21

- Brandenburg, A., Nordlund, A., Stein, R. F., & Torkelsson, U. 1995, *ApJ*, 446, 741
- Brauer, F., Dullemond, C. P., & Henning, T. 2008, *A&A*, 480, 859
- Carballido, A., Bai, X.-N., & Cuzzi, J. N. 2011, *MNRAS*, 415, 93
- Carballido, A., Fromang, S., & Papaloizou, J. 2006, *MNRAS*, 373, 1633
- Cassen, P., & Moosman, A. 1981, *Icar*, 48, 353
- Chapman, S., & Cowling, T. G. 1970, *The Mathematical Theory of Non-uniform Gases. An Account of the Kinetic Theory of Viscosity, Thermal Conduction and Diffusion in gases* (3rd ed.; Cambridge: Univ. Press)
- Cuzzi, J. N., Hogan, R. C., & Shariff, K. 2008, *ApJ*, 687, 1432
- Desch, S. J. 2007, *ApJ*, 671, 878
- Dominik, C., Blum, J., Cuzzi, J. N., & Wurm, G. 2007 in *Protostars and Planets V* ed. B. Reipurth, D. Jewitt, & K. Keil (Tucson, AZ: Univ. Arizona Press), 783
- Dubrulle, B., Morfill, G., & Sterzik, M. 1995, *Icar*, 114, 237
- Dzyurkevich, N., Flock, M., Turner, N. J., Klahr, H., & Henning, T. 2010, *A&A*, 515, A70
- Fedele, D., van den Ancker, M. E., Henning, T., Jayawardhana, R., & Oliveira, J. M. 2010, *A&A*, 510, A72
- Flock, M., Dzyurkevich, N., Klahr, H., Turner, N. J., & Henning, T. 2011, *ApJ*, 735, 122
- Flock, M., Dzyurkevich, N., Klahr, H., Turner, N., & Henning, T. 2012, *ApJ*, 744, 144
- Fromang, S., & Stone, J. M. 2009, *A&A*, 507, 19
- Guan, X., Gammie, C. F., Simon, J. B., & Johnson, B. M. 2009, *ApJ*, 694, 1010
- Haisch, K. E., Jr., Lada, E. A., & Lada, C. J. 2001, *ApJL*, 553, 153
- Hayashi, C. 1981, *PThPS*, 70, 35
- Heinemann, T., & Papaloizou, J. C. B. 2009, *MNRAS*, 397, 64
- Ida, S., Guillot, T., & Morbidelli, A. 2008, *ApJ*, 686, 1292
- Johansen, A., Klahr, H., & Henning, T. 2011, *A&A*, 529, A62
- Johansen, A., Oishi, J. S., Mac Low, M.-M., et al. 2007, *Natur*, 448, 1022
- Johansen, A., & Youdin, A. 2007, *ApJ*, 662, 627
- Johansen, A., Youdin, A., & Klahr, H. 2009a, *ApJ*, 697, 1269
- Johansen, A., Youdin, A., & Mac Low, M.-M. 2009b, *ApJL*, 704, 75
- Klahr, H. H., & Lin, D. N. C. 2001, *ApJ*, 554, 1095
- Kopal, Z. 1989, *The Roche Problem and its Significance for Double-star Astronomy* (Astrophysics and Space Science Library, Vol. 152; Dordrecht: Kluwer)
- Krumholz, M. R., Klein, R. I., & McKee, C. F. 2012, *ApJ*, 754, 71
- Lodders, K. 2003, *ApJ*, 591, 1220
- Lyra, W., Johansen, A., Klahr, H., & Piskunov, N. 2008, *A&A*, 479, 883
- Nakagawa, Y., Sekiya, M., & Hayashi, C. 1986, *Icar*, 67, 375
- Pan, L., Padoan, P., Scalo, J., Kritsuk, A. G., & Norman, M. L. 2011, *ApJ*, 740, 6
- Pinilla, P., Birnstiel, T., Ricci, L., et al. 2012, *A&A*, 538, A114
- Safronov, V. S. (ed.) 1969, *Evolutsiia doplanetnogo oblaka* (English transl.: Evolution of the Protoplanetary Cloud and Formation of Earth and the Planets, NASA Tech. Transl. F-677, 1972.; Jerusalem: Israel Sci. Transl.)
- Shakura, N. I., & Sunyaev, R. A. 1973, *A&A*, 24, 337
- Simon, J. B., Beckwith, K., & Armitage, P. J. 2012, *MNRAS*, 422, 2685
- Sorathia, K. A., Reynolds, C. S., Stone, J. M., & Beckwith, K. 2012, *ApJ*, 749, 189
- Stone, J. M., & Gardiner, T. A. 2010, *ApJS*, 189, 142
- Tsiganis, K., Gomes, R., Morbidelli, A., & Levison, H. F. 2005, *Natur*, 435, 459
- Uribe, A. L., Klahr, H., Flock, M., & Henning, T. 2011, *ApJ*, 736, 85
- von Neumann, J., & Richtmyer, R. D. 1950, *JAP*, 21, 232
- Weidenschilling, S. J. 1977a, *MNRAS*, 180, 57
- Weidenschilling, S. J. 1977b, *Ap&SS*, 51, 153
- Weidenschilling, S. J. 1997, *Icar*, 127, 290
- Whipple, F. L. 1972, in *Proc. Twenty-First Nobel Symp. on From Plasma to Planet*, ed. A. Evlius (New York: Wiley), 211
- Windmark, F., Birnstiel, T., Güttler, C., et al. 2012a, *A&A*, 540, A73
- Windmark, F., Birnstiel, T., Ormel, C. W., & Dullemond, C. P. 2012b, *A&A*, 544, L16
- Youdin, A., & Johansen, A. 2007, *ApJ*, 662, 613
- Youdin, A. N., & Goodman, J. 2005, *ApJ*, 620, 459
- Youdin, A. N., & Lithwick, Y. 2007, *Icar*, 192, 588
- Zsom, A., Ormel, C. W., Güttler, C., Blum, J., & Dullemond, C. P. 2010, *A&A*, 513, A57